


SIMS Bias on Isotope Ratios in Ca-Mg-Fe Carbonates (Part III): $\delta^{18}\text{O}$ and $\delta^{13}\text{C}$ Matrix Effects Along the Magnesite–Siderite Solid-Solution Series

Maciej G. Śliwiński (1, 2)* , Kouki Kitajima (1, 2, 3), Michael J. Spicuzza (1, 2), Ian J. Orland (1, 2), Akizumi Ishida (1, 2, 3, 4), John H. Fournelle (2) and John W. Valley (1, 2, 3)

(1) Department of Geoscience, WiscSIMS, University of Wisconsin-Madison, Madison, WI, 53706, USA

(2) Department of Geoscience, University of Wisconsin-Madison, Madison, WI, 53706, USA

(3) Department of Geoscience, NASA Astrobiology Institute, University of Wisconsin-Madison, Madison, WI, 53706, USA

(4) Department of Earth Science, Tohoku University, Sendai, 9808578, Japan

* Corresponding author. e-mail: msliwinski@wisc.edu

This study explores the effects of cation composition on mass bias (i.e., the matrix effect), which is a major component of instrumental mass fractionation (IMF) in the microanalyses of $\delta^{13}\text{C}$ and $\delta^{18}\text{O}$ by SIMS in carbonates of the magnesite–siderite solid-solution series ($\text{MgCO}_3\text{--FeCO}_3$). A suite of twelve calibration reference materials (RMs) was developed and documented (calibrated range: $\text{Fe}\# = 0.002\text{--}0.997$, where $\text{Fe}\# = \text{molar Fe}/[\text{Mg} + \text{Fe}]$), along with empirical expressions for regressing calibration data (affording residuals $< 0.5\%$ relative to certified reference material NIST-19). The calibration curves of both isotope systems are non-linear and have, over a 2-year period, fallen into one of two distinct but largely self-consistent shape categories (data from ten measurement sessions), despite adherence to well-established analytical protocols for carbonate $\delta^{13}\text{C}$ and $\delta^{18}\text{O}$ analyses at WiscSIMS (CAMECA IMS 1280). Mass bias was consistently most sensitive to changes in composition near the magnesite end-member ($\text{Fe}\# 0\text{--}0.2$), deviating by up to 4.5‰ ($\delta^{13}\text{C}$) and 14‰ ($\delta^{18}\text{O}$) with increasing Fe content. The cause of variability in calibration curve shapes is not well understood at present and demonstrates the importance of having available a sufficient number of well-characterised RMs so that potential complexities of curvature can be adequately delineated and accounted for on a session-by-session basis.

Keywords: SIMS, carbon isotopes, oxygen isotopes, siderite, magnesite, matrix effects, carbonates.

Received 12 May 17 – Accepted 11 Oct 17

Here, we present the third installment of our ongoing study of instrumental mass fractionation (IMF) and sample matrix effects (collectively referred to throughout as ‘bias’) in the analysis of carbon and oxygen isotope ratios from Ca-Mg-Fe carbonates by secondary ion mass spectrometry (SIMS). Building on early pioneering studies (e.g., Eiler *et al.* 1997a, Valley *et al.* 1997, Riciputi *et al.* 1998, Fayek *et al.* 2001), we recently provided an empirical characterisation of SIMS $\delta^{13}\text{C}$ and $\delta^{18}\text{O}$ bias for the dolomite–ankerite solid-solution series ($\text{Ca-Mg}(\text{CO}_3)_2\text{--CaFe}(\text{CO}_3)_2$) and documented the development of a suite of microanalytical reference materials (RMs; Śliwiński *et al.* 2016a, b). The focus here is on the basic elements of the bias response from carbonate compositions that fall along the complete solid-solution that exists between the siderite (FeCO_3) and

magnesite (MgCO_3) end-members of the Ca-Mg-Fe carbonate ternary (e.g., Chai and Navrotsky 1996, Chang *et al.* 1996). Carbonates of the siderite–magnesite series are encountered in many different geological environments; they occur, for example: (a) as siderite concretions in marine and freshwater sediments (Curtis *et al.* 1972, 1986, Gautier 1982, Postma 1982, Mozley 1989a, b, Curtis 1995); (b) as siderite nodules in wetland soils and sediments of the globe’s humid climatic belts (Ludvigson *et al.* 1998, 2013, Ufnar *et al.* 2004, Sheldon and Tabor 2009, Tabor and Myers 2015); (c) as cements in sandstones and mudstones (Macquaker *et al.* 1997, Morad 1998, Burley and Worden 2003); (d) as ore-grade siderite and magnesite deposits (e.g., Frost 1982, Fernández-Nieto *et al.* 2003); (e) in the extensive banded iron formations (BIFs) of the Precambrian

(e.g., James 1954, Klein 2005, see figures 1 and 2 therein); (f) in association with evaporitic sediments (e.g., Botz and von der Borch 1984, Mayayo *et al.* 1996, Lugli *et al.* 2002, Luzón *et al.* 2009, Sanz-Montero and Rodríguez-Aranda 2012, Mees and Keppens 2013); (g) in carbonatite complexes (i.e., carbonate mineral-rich intrusive or extrusive igneous rock bodies; e.g., Buckley and Woolley 1990); (h) as inclusions in mantle diamonds (e.g., Wang *et al.* 1996, Sobolev *et al.* 1997, Dobrzhinetskaya *et al.* 2001, Kaminsky *et al.* 2013); and (i) as a product of weathering or hydrothermal alteration of igneous and metamorphic rock bodies rich in Ca-Mg-Fe silicate minerals (e.g., olivine, pyroxene, plagioclase, feldspars; e.g., Chang *et al.* 1996 and references therein); such environments are being explored as one of many natural analogues to engineered CO₂ storage (e.g., Power and Southam 2005, Wilson *et al.* 2009, Power *et al.* 2013).

Carbonate compositions of the magnesite–siderite series are found in Martian meteorites (e.g., Eiler *et al.* 2002, Niles *et al.* 2013), where they co-occur with members of the dolomite–ankerite series and other, more unusual compositions (from a terrestrial perspective) that are not constrained to either of these two solid-solutions. Similar compositions have been discovered in hydrothermally altered volcanic

deposits in Spitsbergen (e.g., Treiman *et al.* 2002) and are being explored as potential terrestrial analogues for understanding the formation of Martian carbonates (e.g., Blake *et al.* 2010, Morris *et al.* 2011, Stern *et al.* 2013 and references therein).

The isotopic ratios of carbon and oxygen are widely used in the geosciences as proxies for inferring the conditions of carbonate formation; of interest most commonly is the temperature of mineral precipitation, the source(s) of carbon, and the nature/source of the fluids involved (e.g., marine, meteoric, mixed or hydrothermal waters). Variations in the $\delta^{13}\text{C}$ and $\delta^{18}\text{O}$ signatures of pedogenic (soil) carbonates, for example, are frequently used as indicators of past ecologic and climatic change on the continents (Dworkin *et al.* 2005, Sheldon and Tabor 2009, Suarez *et al.* 2010). As a further example, $\delta^{13}\text{C}$ and $\delta^{18}\text{O}$ records continue to be of interest for gaining insights into the diagenetic and metamorphic history of banded iron formations (e.g., Perry *et al.* 1973, Beukes *et al.* 1989, Beukes and Klein 1990, Kaufman *et al.* 1990, Heimann *et al.* 2010), as well as to make inferences about the unique palaeoenvironmental conditions under which they formed, at least in so far as iron formation carbonates constitute a suitable proxy for the chemistry of ancient seawater and atmospheric CO₂

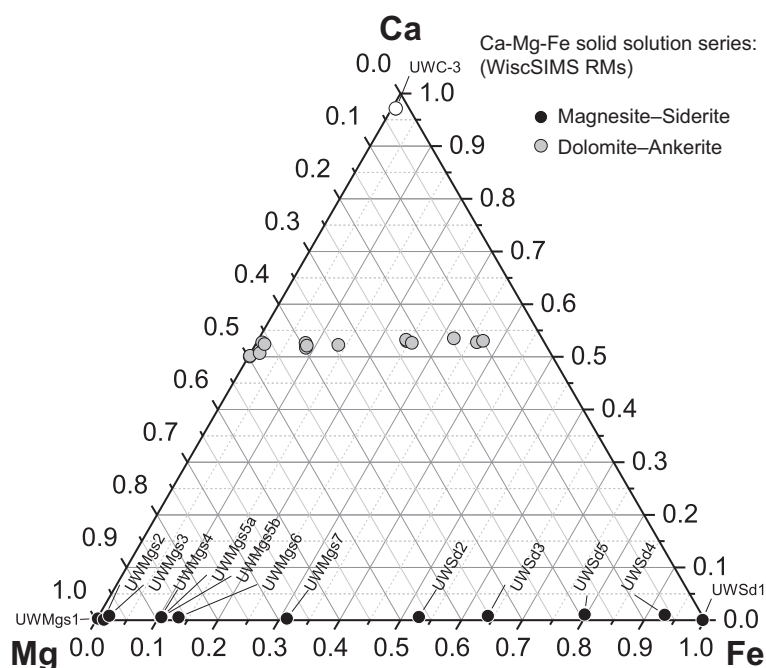


Figure 1. Ternary diagram showing the range of Ca-Mg-Fe carbonate compositions represented by the micro-analytical reference materials developed at WiscSIMS for calibrating SIMS $\delta^{18}\text{O}$ and $\delta^{13}\text{C}$ analyses (Table 1): magnesite–siderite series (this study); dolomite–ankerite series (reported in Śliwiński *et al.* 2016a, b) and calcite UWC-3 (Kozdon *et al.* 2009). Symbols represent average values (associated 2SE values smaller than symbols).

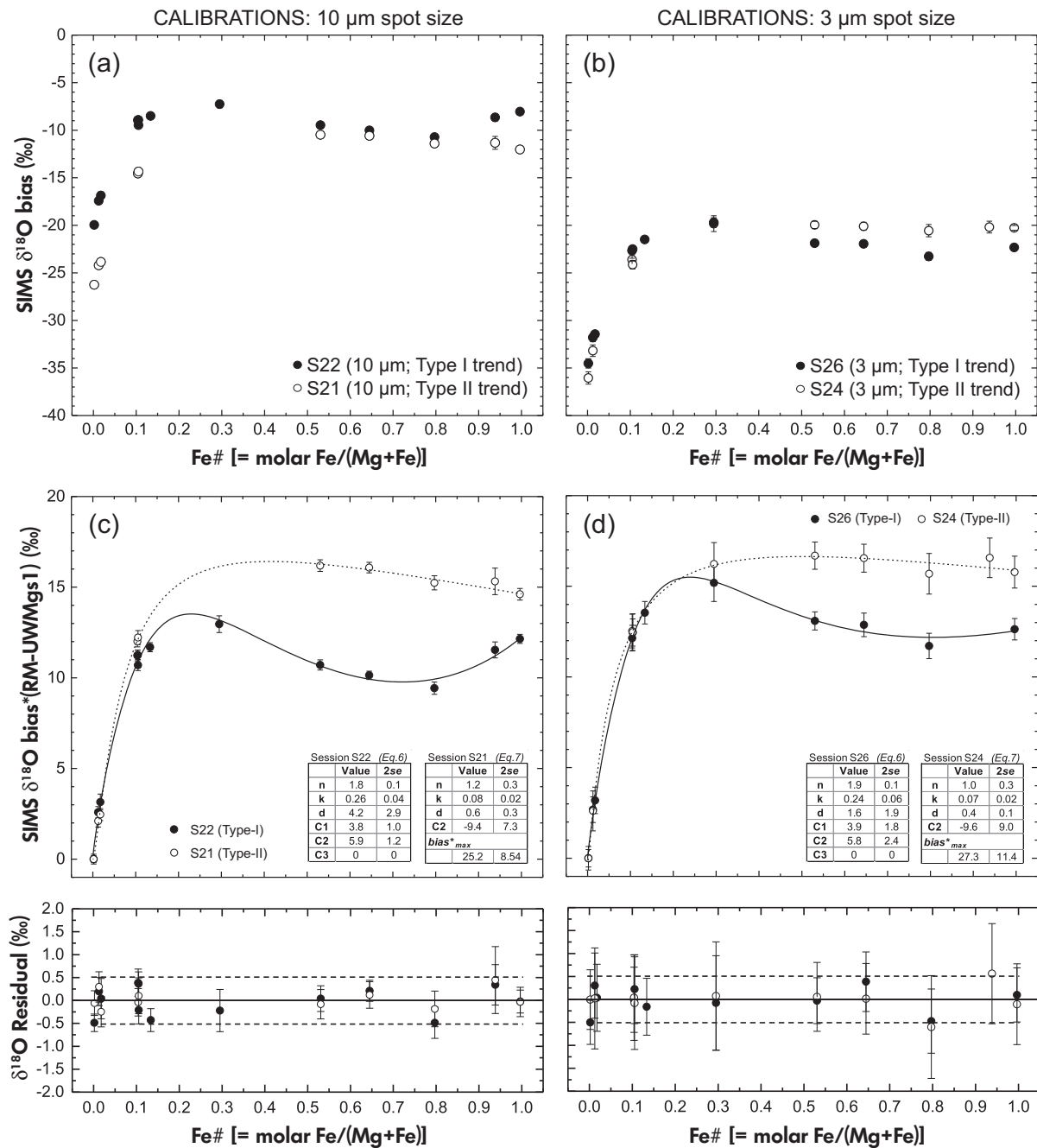


Figure 2. (a, b) Plot relating SIMS $\delta^{18}\text{O bias (}\%)$ to the cation composition of carbonates belonging to the siderite–magnesite solid-solution series [$\text{Fe\#} = \text{Fe}/(\text{Mg} + \text{Fe})$, molar]. Shown are representative examples of two types of bias behaviour observed using consistent analytical protocols for: (a) 10- μm diameter spot-size measurements and (b) 3- μm measurements. (c, d) Working calibration curves based on the data plotted in (a, b), where bias values are normalised to end-member magnesite (expressed as $\delta^{18}\text{O bias}^*(\text{RM-UWMgs1})$), which serves as the calibration anchor. Immediately below are the calibration residuals, which can be considered a measure of accuracy relative to the CRM NIST-19. Refer to Appendix S4 for additional calibration examples.

levels (see Heimann *et al.* 2010, Johnson *et al.* 2013). In many cases, however, the ‘full range’ of isotope values within a sample (or some close approximation thereof) cannot be

resolved and interpreted due to the technical limitations of the sampling methods employed in conventional isotope ratio mass spectrometry. This commonly involves generating

sample powders by microdrilling domains that are hundreds of micrometres in diameter (leading to potential signal averaging effects, especially in instances where multiple carbonate phases are present and crystal size is small).

The motivation for this research grew out of a need for RMs in the wake of recent technical advances in carbonate $\delta^{13}\text{C}$ and $\delta^{18}\text{O}$ microanalysis by SIMS, and the potential applicability of this technique to intensifying research efforts concerned with geological carbon sequestration (McGrail *et al.* 2016, Śliwiński *et al.* 2017). Isotope ratios in carbonates can now be routinely measured *in situ* from micrometre-scale sample domains with sub per mil (‰) repeatability (*sensu* VIM 2008, 2.20 and 2.21; Valley and Kita 2009). The accuracy of measurement (*sensu* VIM 2008, 2.13) in relation to a certified reference material (e.g., NIST-19), however, depends in large part on the availability and overall quality of matrix-matched RMs. That is, accuracy is limited by the extent to which RMs are chemically and isotopically homogenous on the spatial scale of intended use, and a sufficient number of these are needed to adequately characterise bias as a function of chemical composition (e.g., Hervig *et al.* 1992, Valley and Kita 2009). For many mineral families wherein the compositional end-members form extensive or complete solid-solutions with one-another – such as the carbonates – proper standardisation remains a work in-progress for the community of SIMS laboratories around the world.

Methods

The methodology employed is documented in detail in the first two parts of this study (Śliwiński *et al.* 2016a, b). Thus, only a skeletal outline is provided here. Clean grain splits (425–710 μm size fraction) of thirty-eight different naturally-occurring carbonate mineral specimens of the magnesite–siderite series (Table 1) were prepared after extracting approximately one-half to 1 cm^3 of the clearest or most visually uniform domain of each sample. A suite of polished grain mounts was prepared, and all thirty-eight test materials were first evaluated for chemical zoning by BSE-SEM imaging (each grain mount contained twenty randomly selected grains of five different specimens). The most visually uniform test materials (seventeen of the thirty-eight in total) were then assessed by EPMA for variance in chemical composition (typically three spot analyses randomly placed on each of twenty grains) and later by SIMS to determine the extent of $\delta^{18}\text{O}$ and $\delta^{13}\text{C}$ uniformity (typically one spot on each of twenty grains). SIMS measurements were made using the CAMECA IMS 1280 large radius multi-collector ion microprobe at the WiscSIMS Laboratory, Department of Geoscience, University of Wisconsin-Madison). Thirteen of these test materials (Table 1) were considered acceptable

and lastly analysed by conventional phosphoric acid digestion (12 h, 100 °C) and gas source mass spectrometry (McCrea 1950) to calibrate the average $\delta^{13}\text{C}$ and $\delta^{18}\text{O}$ values relative to VPDB and VSMOW, respectively. In each case, a single 25–50 mg subsample of grains was powdered, and three separate digestions were performed on ~ 5-mg splits. Phosphoric acid-fractionation factors for $\delta^{18}\text{O}$ measurements were calculated based on composition using the formulation of Rosenbaum and Sheppard (1986).

Chemical homogeneity evaluations by EPMA were performed using either a 1-, 5- or 10- μm diameter beam (CAMECA SX-51 or SXFive FE, operated at 15 keV and 10–20 nA; see Appendix S2 for RM-specific details). Fluorescent X-ray signals on all spectral peak positions (Mg, Ca, Mn and Fe-K α peaks, Sr-L α) were measured for either 60 or 120 s. The guiding principle was to acquire at least 10,000 background-corrected Fe-K α or Mg-K α counts from the near end-member compositions that contain low concentrations of these elements (< 2 mol%); this ensures that the relative standard deviation associated with X-ray counting statistics remains below 1%. Spectral background corrections were implemented using the Mean Atomic Number (MAN) method described by Donovan and Tingle (1996). During the course of a point analysis, the intensities of characteristic X-rays fluorescing from electron beam-sensitive materials can drift; this effect was monitored and corrected by a feature in Probe for EPMA software (Donovan *et al.* 2007) called ‘TDI’ (time-dependent intensity), where data plotted in *measured X-ray intensity* vs. *time* space are de-trended before ZAF corrections are applied.

A note on terminology and data presentation

Measurements of carbon and oxygen isotope ratios in carbonate minerals by SIMS are affected by systematic inaccuracies arising from mass fractionation effects, a component of which is instrumental in nature. Fractionation occurs as follows: (a) during secondary ion formation at the sample surface (sputtering); (b) during uptake and transmission through the mass spectrometer; and then again (c) during detection (e.g., Hervig *et al.* 1992, Eiler *et al.* 1997b, Fitzsimons *et al.* 2000, Valley and Kita 2009, Huberty *et al.* 2010). A further component of mass fractionation is related to sample composition, which varies systematically in minerals that exhibit solid-solution behaviour (i.e., the sample matrix effect; e.g., Eiler *et al.* 1997a, b, Riciputi *et al.* 1998, Page *et al.* 2010, Ickert and Stern 2013, Kitajima *et al.* 2015, Śliwiński *et al.* 2016a, b).

For a given SIMS configuration, these collective effects can be highly consistent across analytical sessions spread

Table 1. Source locality and measured extent of $\delta^{18}\text{O}$ and $\delta^{13}\text{C}$ homogeneity on the microanalytical scale of SIMS (10 and 6- μm scale, respectively) in the magnesite-siderite RMs of this study

RM ID	Fe#	Source locality	True $^{\alpha}$ $\delta^{18}\text{O}$ (‰, VSMOW)	True $^{\alpha}$ $\delta^{13}\text{C}$ (‰, VPDB)	SIMS $\delta^{18}\text{O}$ homogeneity assessment				SIMS $\delta^{13}\text{C}$ homogeneity assessment					
					Session ID	Grains (n)	Analyses (n)	2s	2SE	Session ID	Grains (n)	Analyses (n)	2s	2SE
UWMgs1	0.002	Bumado District, Brazil	12.28	-0.82	S19	20	20	0.34	0.08	S20	20	20	0.84	0.19
UWMgs2	0.012	Italy (no additional details known)	16.99	-5.03	S19	19	20	0.46	0.10	S20	19	20	0.88	0.20
UWMgs3 ^b	0.017	Steiermark, Austria	10.58	-0.32	S19	21	25	0.86	0.17	S20	20	20	0.99	0.22
UWMgs4	0.104	(Oberdorf an der Laming?) Cassette, Chester, Windsor Co., Vermont, USA	12.62	-11.97	S19	19	20	0.32	0.07	S20	19	20	1.00	0.22
UWMgs5a ^c	0.105	Val di Vizze, Trentino-Alto Adige, Bolzano, Italy	11.01	-4.92	S19	19	20	0.44	0.10	S20	19	20	0.90	0.20
UWMgs5b ^c	0.105	Val di Vizze, Trentino-Alto Adige, Bolzano, Italy	11.01	-4.90	S19	20	20	0.36	0.08	–	–	–	–	–
UWMgs6 ^b	0.134	Adige River (upper part of); Val di Vizze, Trentino-Alto Adige, Bolzano, Italy	10.94	-4.95	S16	15	23	0.69	0.14	S17	15	23	1.02	0.21
UWMgs7 ^d	0.295	Savage River mine area, Tasmania, Australia	16.61	1.35	S22	22	23	1.89	0.39	S23	17	20	0.92	0.20
UWSd2	0.530	Morro Velho Mine, Nova Lima, Minas Gerais, Brazil	15.88	-4.03	S16	17	20	0.36	0.08	S18	17	20	0.46	0.10

Table 1 (continued).
Source locality and measured extent of $\delta^{18}\text{O}$ and $\delta^{13}\text{C}$ homogeneity on the microanalytical scale of SIMS (10 and 6- μm scale, respectively) in the magnesite-siderite RMs of this study

RM ID	Fe#	Source locality	True ^a $\delta^{18}\text{O}$ (‰, VSMOW)	True ^a $\delta^{13}\text{C}$ (‰, VPDB)	SIMS $\delta^{18}\text{O}$ homogeneity assessment				SIMS $\delta^{13}\text{C}$ homogeneity assessment					
					Session ID	Grains (n)	Analyses (n)	2s	2SE	Session ID	Grains (n)	Analyses (n)	2s	2SE
UWSd3	0.645	Morro Velho Mine, Nova Lima, Minas Gerais, Brazil	15.30	-5.06	S16	17	20	0.25	0.06	S18	17	21	0.72	0.16
UWSd4 ^b	0.938	Mount St. Hilaire, Quebec, Canada	9.14	-5.49	S16	23	22	0.81	0.17	S18	20	20	0.85	0.19
UWSd5	0.797	Locality unknown	10.48	-7.28	S16	19	21	0.56	0.12	S20	18	19	0.90	0.21
UWSd1	0.997	Ivigut Cryolite deposit, Mittuut (Ivigut), Atsuk Fjord, Sermersooq, Greenland	7.92	-8.07	S19	20	20	0.36	0.08	S20	20	20	0.59	0.13

^a $\delta^{18}\text{O}$ and $\delta^{13}\text{C}$ VSMOW value determined by conventional phosphoric acid digestion and gas-source mass spectrometry (see Appendix S1).

^b Denotes an RM which may be used for $\delta^{18}\text{O}$ calibration only if analysed repeatedly a sufficient number of times to drive the standard error (at the 95% confidence level) below 0.3‰ (approx. $n = 8$).

^c Two separate splits of this material were evaluated.

^d This RM is not preferred for routine use in $\delta^{18}\text{O}$ calibration. Approx. 25⁺ replicate measurements are required to drive the standard error to approx. 0.3‰.

over a multiyear period (Śliwiński *et al.* 2016a, b). Throughout this article, we will refer to the sum total of these effects as the $\delta^{18}\text{O}$ and $\delta^{13}\text{C}$ 'bias'. As defined by the International Vocabulary of Metrology (VIM 2008), 'measurement bias' is an 'estimate of a systematic measurement error' (2.18, VIM 2008), the effects of which can be compensated for by a correction or calibration. A systematic measurement error, the causes of which can be known or unknown, is the 'component of measurement error that in replicate measurements remains constant or varies in a predictable manner (2.17, VIM 2008)'.

At present, secondary ion yields and the bias imparted to isotope ratios during sputtering cannot be accurately predicted from first principles for naturally occurring minerals and glasses. Further, the relative contributions of instrumental vs. sample matrix effects to the total measurement bias are unknown (see, however, the work of Fàbrega *et al.* 2017). Nonetheless, carbonate $\delta^{18}\text{O}$ and $\delta^{13}\text{C}$ values can be determined accurately by SIMS with proper standardisation. Critically, bias can vary from session to session due to variations in instrumental parameters. For carbonate solid-solutions, this requires a sufficient number of well-characterised RMs to empirically characterise bias as a function of chemical composition on a session-by-session basis.

The bias associated with SIMS measurements of $\delta^{18}\text{O}$ and $\delta^{13}\text{C}$ values from RMs is expressed as follows:

$$\alpha^{18}\text{O}_{\text{SIMS}} = \frac{1 + (\delta^{18}\text{O}_{\text{raw}}/1000)}{1 + (\delta^{18}\text{O}_{\text{VSMOW}}/1000)} \quad (1)$$

$$\alpha^{13}\text{C}_{\text{SIMS}} = \frac{1 + (\delta^{13}\text{C}_{\text{raw}}/1000)}{1 + (\delta^{13}\text{C}_{\text{VPDB}}/1000)} \quad (2)$$

(modified after Kita *et al.* 2009). For each RM, the terms ' $\delta^{18}\text{O}_{\text{raw}}$ ' and ' $\delta^{13}\text{C}_{\text{raw}}$ ' represent the measured $^{18}\text{O}/^{16}\text{O}$ and $^{13}\text{C}/^{12}\text{C}$ ratios that have been corrected for background, drift and detector dead time (if electron multipliers were used) and respectively normalised to the $^{18}\text{O}/^{16}\text{O}$ ratio in Vienna Standard Mean Ocean Water ($^{18}\text{O}/^{16}\text{O}_{\text{VSMOW}} = 0.00200520$, Baertschi 1976) and the $^{13}\text{C}/^{12}\text{C}$ ratio in the Vienna Pee-Dee Belemnite ($^{13}\text{C}/^{12}\text{C}_{\text{VPDB}} = 0.0112372$; Craig 1957, Allison *et al.* 1995). They are thus expressed in the customary way as per mil deviations (‰; δ notation) from the accepted values of the VSMOW and VPDB certified reference materials (CRMs). However, both terms are bias-uncorrected and are therefore not accurate relative to VSMOW and VPDB. The terms ' $\delta^{18}\text{O}_{\text{VSMOW}}$ ' and ' $\delta^{13}\text{C}_{\text{VPDB}}$ ', on the other hand, represent the average $\delta^{18}\text{O}$ and $\delta^{13}\text{C}$ values of the same RM that have been independently calibrated to the

VSMOW and VPDB scales by conventional phosphoric acid digestion and gas source mass spectrometric analysis.

Values of $\alpha^{18}\text{O}_{\text{SIMS}}$ and $\alpha^{13}\text{C}_{\text{SIMS}}$ (Equations 1 and 2) are generally close to unity and are therefore consistently expressed throughout this article using δ -notation and referred to as the ' $\delta^{18}\text{O}$ bias' and ' $\delta^{13}\text{C}$ bias', respectively:

$$\text{bias} = 1000 \cdot (\alpha - 1) \quad (3)$$

where α is either $\alpha^{18}\text{O}_{\text{SIMS}}$ or $\alpha^{13}\text{C}_{\text{SIMS}}$.

All equations presented here are formulated such that all mathematical operations involving multiplication or division are performed on α terms, explicitly avoiding the common approximation where: $\delta_A - \delta_B \cong 1000 \ln(\alpha_{A-B})$. Thus, for example, if two or more isotope ratios expressed using δ -notation are to be multiplied and/or divided, they are first converted to α values, multiplied and/or divided, and finally converted back to isotope δ values.

In order to construct working calibration curves that relate bias to chemical composition, the $\delta^{18}\text{O}$ and $\delta^{13}\text{C}$ bias of each RM was normalised (or 'anchored') to that of end-member magnesite (UWMgs1):

$$\begin{aligned} &\delta^{13}\text{C} \text{ or } \delta^{18}\text{O} \text{ bias}^*(\text{RM} - \text{UWMgs1}) \\ &= 1000 \cdot \left[\frac{1 + (\text{bias}_{\text{RM}}/1000)}{1 + (\text{bias}_{\text{UWMgs1}}/1000)} - 1 \right] \quad (4) \end{aligned}$$

The '*' symbol indicates a normalised bias value. The associated propagation of analytical uncertainties is of the same general form as that reported in Śliwiński *et al.* (2016a, appendix S5 therein).

In cross-plotting and examining $\delta^{13}\text{C}$ and $\delta^{18}\text{O}$ bias as a function of cation chemistry of the magnesite–siderite series, the composition is consistently expressed as the Fe/(Mg + Fe) molar ratio (i.e., the Fe#).

Uncertainties associated with SIMS $\delta^{13}\text{C}$ and $\delta^{18}\text{O}$ measurements are reported in one of two ways:

- (1) As a standard deviation value (at the 95% confidence level) for a sample of a population ($2s = 2\sqrt{\Sigma(x - \bar{x})^2/(n - 1)}$, where \bar{x} is the average (statistical mean) of a set of n values). This is relevant in reporting: (a) the level of isotopic homogeneity of each evaluated RM (where the intent is to show the extent to which individual

measurements are spread about the mean), and (b) the measurement precision for a single sample spot analysis (based on the 2s value of eight repeat measurements of a drift-monitoring material that brackets each set of ~ 10 sample measurements).

- (2) As a standard error of the mean (at the 95% confidence level) for a sample of a population ($2SE = 2s/\sqrt{n}$, where n is the number of observations). This is particularly relevant to calibration diagrams, where the 2SE value reflects upon how well the average is known for each set of replicate RM measurements. As the number of replicate measurements (n) increases, the average value calculated for each RM becomes a more reliable estimate of each respective population average. Uncertainties associated with regression parameters are also expressed as 2SE values. A useful review of the uncertainties associated with SIMS measurements can be found, for example, in Fitzsimons *et al.* (2000).

Results and discussion

Summary of chemical homogeneity assessments

The calibration suite consists of twelve reference materials (see Table 1). The complete solid-solution that exists between the magnesite ($MgCO_3$) and siderite ($FeCO_3$) end-members is uniformly represented by eleven different carbonate compositions ($Fe\#$ 0.002 to 0.997; see Table 2). Note that two of the materials sourced from different localities (UWMgs4 and 5a, b) share a similar cation chemistry but are isotopically dissimilar (making for twelve RMs in total). Variability in the molar $Fe/(Mg + Fe)$ ratio (i.e., $Fe\#$) is as small as 0.001 (2s) and does not exceed 0.022 (2s) $Fe\#$ units. For most RMs in the suite, the relative standard measurement uncertainty ($100 \times 2s/\text{average}$; 95% confidence level) falls between 0.1 and 13.7%. The relatively high value (33.6%) associated with UWMgs2 – which contains 1.25% $FeCO_3$ – reflects greater chemical heterogeneity compared with all other RMs in the suite, requiring a larger number of replicate analyses for routine use (typically at least eight). In the case of the magnesite end-member (UWMgs1), however, the high-relative standard measurement uncertainty value (49%) is associated with only a trace mass fraction of Fe (0.17% $FeCO_3$), which has no measurable effect on $\delta^{18}O$ or $\delta^{13}C$ bias.

Less than 1% $MnCO_3$ is present in RM compositions near the magnesite end-member ($Fe\# < 0.15$), whereas all others generally contain $< 5\%$ (the one exception is UWSd4, with 8.35%). The entire suite contains up to ~ 1%

$CaCO_3$ and no detectable Sr (detection limit of 0.01% $SrCO_3$). The complete EPMA data set is provided in Appendix S2.

Summary of isotopic homogeneity assessments

The level of isotopic homogeneity of each RM on the microanalytical scale was assessed using a 10- μm diameter spot-size for $\delta^{18}O$ and a 6- μm spot-size for $\delta^{13}C$ measurements. Typically, approximately twenty different grains were analysed once each.

Of the twelve RMs in total, eight yielded $\delta^{18}O$ data sets with $2s < 0.56\%$ (see Table 1). An additional three RMs yielded 2s values $< 0.86\%$ and are considered to be routinely usable for calibration if the 2SE value is driven to $\approx 0.3\%$ with a sufficient number of replicate measurements (approximately eight measurements are required in this case from a handful of grains, whereas more uniform RMs require as little as four). For reference consider that a 2s value of 0.3% is expected for $n = 4$ replicate measurements performed on a nominally homogenous material; this is based on considerations of ion counting statistics, overall instrument stability and slight mount-specific differences in $\delta^{18}O$ bias values measured from drift-monitoring materials (e.g., Kita *et al.* 2009, Valley and Kita 2009). In the case of RMs with slight heterogeneity, a 2s value of up to approximately $\pm 0.5\%$ is considered acceptable. Reference material UWMgs7 is not preferred for routine use on account of a 2s value of 1.89% and the large number of replicate measurements (> 20) required to drive the 2SE value to 0.4%. However, data for this material are being presented because it nonetheless provides critical insight into the magnitude of SIMS $\delta^{18}O$ bias in the compositional range between $Fe\#$ 0.2 and 0.4, for which it was difficult to obtain samples in sufficient quantity for RM development.

All twelve RMs yielded $\delta^{13}C$ data sets with 2s values $< 1.0\%$ (2s; Table 1). Based on the same considerations as above, a 2s value of 0.6–1.2% is expected for $n = 4$ replicate measurements using the instrumental configuration and analytical protocol employed at WiscSIMS for small-spot carbonate $\delta^{13}C$ analyses (6- μm diameter spot-size). Please note that in comparison with oxygen, measurements of carbon isotope ratios are inherently more variable because: (a) carbon has a lower ionisation efficiency than oxygen under comparable primary ion beam conditions, and (b) carbon comprises only 20% of all atoms in the carbonate crystal structure (compared with oxygen which accounts for 60%), requiring the use of an electron multiplier for detecting the secondary $^{13}C^-$ ion stream.

Table 2. Average chemical composition of the magnesite–siderite RMs of this study (analysed by EPMA)

RM ID	Grains (n)	EPMA analyses (n)	%MgCO ₃	2s (%)	%CaCO ₃	2s (%)	%FeCO ₃	2s (%)	%MnCO ₃	2s (%)	%SiCO ₃	2s	Fe# (Fe/(Mg+Fe))	2s	2SE	Fe# (with Mn)	2s	2SE	Fe (% m./m)	2s	2SE
UWMgs1	20	60	99.47	0.27	0.29	0.31	0.17	0.08	0.07	0.03	< DL	0.002	0.002	0.001	0.000	0.002	0.001	0.000	0.11	0.05	0.000
UWMgs2	19	57	98.66	0.47	0.09	0.08	1.25	0.42	0.02	0.02	< DL	0.004	0.012	0.004	0.001	0.013	0.004	0.001	0.80	0.27	0.001
UWMgs3	21	63	97.29	1.30	0.84	1.34	1.73	0.23	0.14	0.04	< DL	0.017	0.017	0.002	0.000	0.019	0.002	0.000	1.11	0.15	0.000
UWMgs4	19	57	88.65	0.35	0.54	0.11	10.29	0.34	0.51	0.09	< DL	0.104	0.104	0.003	0.000	0.109	0.003	0.000	6.41	0.23	0.000
UWMgs5a ^a	21	61	88.26	0.82	0.55	0.18	10.39	1.16	0.80	0.26	< DL	0.105	0.105	0.009	0.001	0.113	0.009	0.001	6.46	0.72	0.001
UWMgs5b ^a	19	57	88.30	0.72	0.55	0.20	10.36	1.05	0.79	0.23	< DL	0.105	0.105	0.010	0.001	0.112	0.008	0.001	6.44	0.64	0.001
UWMgs6	15	46	85.76	1.63	0.52	0.15	13.22	1.84	0.50	0.16	< DL	0.134	0.134	0.018	0.003	0.138	0.017	0.003	8.13	1.10	0.003
UWMgs7	21	65	68.52	1.32	0.29	0.18	28.64	1.11	2.56	0.37	< DL	0.295	0.295	0.012	0.001	0.313	0.013	0.002	16.80	0.63	0.002
UW5d2	16	48	46.10	0.84	0.59	0.39	52.07	0.96	1.24	0.17	< DL	0.530	0.530	0.009	0.001	0.536	0.009	0.001	28.39	0.62	0.001
UW5d3	17	51	33.47	2.07	0.77	0.18	60.76	2.29	5.00	0.33	< DL	0.645	0.645	0.023	0.003	0.663	0.021	0.003	32.05	1.08	0.003
UW5d4	21	61	5.58	1.36	0.93	1.03	85.14	3.89	8.35	2.27	< DL	0.938	0.938	0.016	0.002	0.944	0.014	0.002	41.84	1.74	0.002
UW5d5	19	53	19.21	2.35	1.07	0.49	75.46	1.85	4.25	1.65	< DL	0.797	0.797	0.022	0.003	0.806	0.023	0.003	38.02	1.02	0.003
UW5d1	22	69	0.33	0.10	0.03	0.02	95.34	0.29	4.32	0.24	< DL	0.997	0.997	0.001	0.000	0.997	0.001	0.000	46.23	0.58	0.000

^a Replicate splits.

Replicate $\delta^{18}\text{O}$ and $\delta^{13}\text{C}$ measurements of mg-sized grain splits of each RM by phosphoric acid digestion and gas source mass spectrometry yielded 2s values no larger than 0.14‰ and 0.04‰, respectively (Appendix S1). The range of $\delta^{18}\text{O}$ values represented by the entire suite extends from 7.92 to 16.99‰ VSMOW (-22.30 to -13.50‰ VPDB), whereas the $\delta^{13}\text{C}$ range extends from -11.97 to -0.32‰ VPDB. The complete SIMS data set is provided in Appendix S3.

Calibrations (overview)

In the first two parts of this study, we empirically constrained the behaviour of SIMS $\delta^{18}\text{O}$ and $\delta^{13}\text{C}$ bias for carbonate mineral compositions of the dolomite–ankerite solid-solution series and introduced the use of a Hill-type equation (Hill 1910, Goutelle *et al.* 2008) as an adequate means of mathematically modelling the highly non-linear distribution of calibration data in composition vs. bias space (Equation (4) in Śliwiński *et al.* 2016a, b):

$$\delta^{18}\text{O or } \delta^{13}\text{C bias}^* (\text{RM} - \text{RM}_{\text{end-member dolomite}}) = \frac{(\text{Bias}_{\text{max}}^*)x^n}{k^n + x^n} \quad (5)$$

where 'x' = Fe#, 'k' and 'n' are curve-shape parameters and 'Bias*_{max}' is an analytical session-specific scaling factor. Note that the bias of each RM is normalised to that of an end-member dolomite ('UW6220' at WiscSIMS), which serves as the 'anchor' for the dolomite–ankerite series (the asterisk denotes that bias values have been normalised to the calibration anchor). Under routine operating conditions for carbonate $\delta^{18}\text{O}$ and $\delta^{13}\text{C}$ analysis at WiscSIMS, this equation has been reliably applied over a 3-year period using the same set of curve-shape parameter values to regress calibration data acquired using: (a) 10- μm spot-size $\delta^{18}\text{O}$ analysis conditions; (b) 3- μm spot-size $\delta^{18}\text{O}$ conditions; and (c) 6- μm spot-size $\delta^{13}\text{C}$ conditions (additional calibration data sets have been acquired since publication of Parts I and II of this study—e.g., Brodie 2016, Haroldson 2017—but no significant changes in the values of the curve-shape parameters have been observed).

Unlike the dolomite–ankerite bias calibrations, the magnesite–siderite trends have unexpectedly behaved less consistently from session to session and have shown more complexity of curvature. Throughout the 2-year time span of RM development, we have acquired calibration data for the magnesite–siderite series on multiple occasions; the data set presented here includes measurements from: (a) four separate 10- μm spot-size $\delta^{18}\text{O}$ sessions; (b) two 3- μm $\delta^{18}\text{O}$ sessions; and (c) four 6- μm $\delta^{13}\text{C}$ sessions (see data

Table 3. SIMS $\delta^{18}\text{O}$ bias data for magnesite-siderite calibration RMs of this study, measured during multiple measurement sessions over a 2-year period (2015–2017)

Session ID	Spot size (μm)	Trend type	RM ID	Fe# ^a	$\delta^{18}\text{O}$ True ^b (%o, VSMOW)	$\delta^{18}\text{O}$ raw ^c	2SE	$\delta^{18}\text{O}$ bias ^{c,d}	2SE	$\delta^{18}\text{O}$ bias*(RM-UWMgs1) ^e	2SE	^{16}O -Yield (Gcps/nA)	2SE	$\Delta^{18}\text{O}$ ($\epsilon_F - \epsilon_I$) ^f	2SE
S16 ^g	10	Type-I	Brazil Mg ^h UWMgs1	0.004	15.01	-4.58	0.02	-19.30	0.02	0.00	0.10	1.791	0.014	-2.84	0.37
S16 ^g	10	Type-I	UWMgs2	0.002	12.28	-	-	-	-	-	-	-	-	-	-
S16 ^g	10	Type-I	UWMgs3	0.012	16.99	-	-	-	-	-	-	-	-	-	-
S16 ^g	10	Type-I	UWMgs4	0.017	10.58	-	-	-	-	-	-	-	-	-	-
S16 ^g	10	Type-I	UWMgs5a	0.104	12.62	-	-	-	-	-	-	-	-	-	-
S16 ^g	10	Type-I	UWMgs5b	0.105	11.01	-	-	-	-	-	-	-	-	-	-
S16 ^g	10	Type-I	UWMgs6	0.105	11.01	-	-	-	-	-	-	-	-	-	-
S16 ^g	10	Type-I	UWMgs7	0.134	10.94	2.17	0.15	-8.68	0.15	11.38	0.19	2.195	0.016	-2.08	0.15
S16 ^g	10	Type-I	UWMgs6	0.295	16.61	-	-	-	-	-	-	-	-	-	-
S16 ^g	10	Type-I	UWSd2	0.530	15.88	6.27	0.08	-9.46	0.08	10.64	0.16	2.869	0.006	-1.11	0.15
S16 ^g	10	Type-I	UWSd3	0.645	15.30	5.05	0.06	-10.09	0.06	10.00	0.15	3.009	0.008	-0.83	0.10
S16 ^g	10	Type-I	UWSd4	0.938	9.14	0.18	0.17	-8.88	0.17	11.21	0.22	2.944	0.082	-2.13	0.21
S16 ^g	10	Type-I	UWSd5	0.797	10.48	-0.40	0.12	-10.77	0.12	9.24	0.18	3.014	0.009	-1.30	0.23
S16 ^g	10	Type-I	UWSd1	0.997	7.92	-	-	-	-	-	-	-	-	-	-
S16 ^g	10	Type-I	lvig. Sd ⁱ	0.998	7.79	-0.46	0.12	-8.18	0.12	11.33	0.16	2.960	0.008	-2.94	0.28
S19	10	Type-I	Brazil Mg ^h UWMgs1	0.004	15.01	-	-	-	-	-	-	-	-	-	-
S19	10	Type-I	UWMgs2	0.002	12.28	-8.33	0.08	-20.36	0.08	0.00	0.19	1.826	0.006	-3.42	0.21
S19	10	Type-I	UWMgs3	0.012	16.99	-1.40	0.10	-18.14	0.10	2.33	0.22	1.874	0.007	-3.24	0.17
S19	10	Type-I	UWMgs4	0.017	10.58	-7.15	0.17	-17.64	0.17	2.78	0.26	1.870	0.007	-3.04	0.15
S19	10	Type-I	UWMgs5a	0.104	12.62	3.21	0.07	-9.37	0.07	11.28	0.25	2.093	0.010	-2.42	0.17
S19	10	Type-I	UWMgs5b	0.105	11.01	1.46	0.10	-9.60	0.10	11.04	0.22	2.060	0.008	-2.50	0.21
S19	10	Type-I	UWMgs6	0.134	10.94	1.76	0.08	-9.50	0.08	11.14	0.21	2.052	0.010	-2.24	0.18
S19	10	Type-I	UWMgs7	0.295	16.61	2.60	0.18	-8.71	0.18	11.94	0.28	2.172	0.013	-2.12	0.24
S19	10	Type-I	UWSd2	0.530	15.88	6.56	0.04	-9.43	0.04	11.21	0.21	2.702	0.004	-1.02	0.37
S19	10	Type-I	UWSd3	0.645	15.30	5.36	0.09	-10.04	0.09	10.59	0.22	2.861	0.018	-0.79	0.29
S19	10	Type-I	UWSd4	0.938	9.14	0.38	0.20	-8.93	0.20	11.72	0.29	2.829	0.010	-3.06	0.21
S19	10	Type-I	UWSd5 ⁱ	0.797	10.48	-	-	-	-	-	-	-	-	-	-
S19	10	Type-I	UWSd1 ^k	0.997	7.92	-0.50	0.08	-8.55	0.08	12.11	0.22	2.767	0.005	-3.79	0.14
S19	10	Type-I	lvig. Sd ⁱ	0.998	7.79	-	-	-	-	-	-	-	-	-	-
S21	10	Type-II	Brazil Mg ^h UWMgs1	0.004	15.01	-	-	-	-	-	-	-	-	-	-
S21	10	Type-II	UWMgs2	0.002	12.28	-14.29	0.26	-26.25	0.26	0.00	0.27	1.784	0.019	-2.22	0.26
S21	10	Type-II	UWMgs3	0.012	16.99	-7.63	0.20	-24.21	0.20	2.10	0.33	1.843	0.014	-1.62	0.15
S21	10	Type-II	UWMgs4	0.017	10.58	-13.52	0.20	-23.85	0.20	2.46	0.33	1.860	0.015	-1.49	0.14
S21	10	Type-II	UWMgs5a	0.104	12.62	-2.12	0.13	-14.56	0.13	12.01	0.30	2.283	0.045	-1.20	0.17
S21	10	Type-II	UWMgs5b	0.105	11.01	-3.86	0.26	-14.35	0.26	12.22	0.39	2.439	0.007	-1.00	0.18

Table 3 (continued).
SIMS $\delta^{18}\text{O}$ bias data for magnetite-siderite calibration RMs of this study, measured during multiple measurement sessions over a 2-year period (2015–2017)

Session ID	Spot size (μm)	Trend type	RM ID	Fe# ^a	$\delta^{18}\text{O}$ True ^b (‰, VSMOW)	$\delta^{18}\text{O}$ raw ^c	2SE	$\delta^{18}\text{O}$ bias ^{c,d}	2SE	$\delta^{18}\text{O}$ bias*(RM-UWMgs1) ^e	2SE	^{16}O -Yield (Gcps/nA)	2SE	$\Delta^{18}\text{O}$ ($\epsilon_{\text{P-C}}$) ^f	2SE
S21	10	Type-II	UWMgs5b	0.105	11.01	-	-	-	-	-	-	-	-	-	-
S21	10	Type-II	UWMgs6	0.134	10.94	-	-	-	-	-	-	-	-	-	-
S21	10	Type-II	UWMgs7	0.295	16.61	-	-	-	-	-	-	-	-	-	-
S21	10	Type-II	UWSd2	0.530	15.88	4.83	0.15	-10.48	0.32	16.19	0.024	2.977	0.32	-0.70	0.15
S21	10	Type-II	UWSd3	0.645	15.30	4.14	0.07	-10.59	0.29	16.08	0.016	3.056	0.12	-0.55	0.12
S21	10	Type-II	UWSd4	0.938	9.14	-2.70	0.68	-11.33	0.73	15.32	0.110	3.189	0.17	-0.79	0.17
S21	10	Type-II	UWSd5	0.797	10.48	-1.45	0.28	-11.41	0.39	15.24	0.012	3.080	0.18	-0.38	0.18
S21	10	Type-II	UWSd1 ^k	0.997	7.92	-4.56	0.07	-12.03	0.32	14.61	0.012	3.462	0.15	-1.42	0.15
S21	10	Type-II	lvig- Sd ^l	0.998	7.79	-	-	-	-	-	-	-	-	-	-
S22	10	Type-I	Brazil Mgs ^h	0.004	15.01	-	-	-	-	-	-	-	-	-	-
S22	10	Type-I	UWMgs1	0.002	12.28	-7.93	0.16	-19.96	0.19	0.00	0.008	2.080	0.30	-3.40	0.30
S22	10	Type-I	UWMgs2	0.012	16.99	-0.73	0.24	-17.42	0.31	2.59	0.013	2.121	0.40	-3.40	0.40
S22	10	Type-I	UWMgs3	0.017	10.58	-6.41	0.37	-16.87	0.44	3.15	0.010	2.137	0.30	-3.30	0.30
S22	10	Type-I	UWMgs4	0.104	12.62	3.62	0.08	-8.95	0.30	11.23	0.012	2.368	0.40	-2.30	0.40
S22	10	Type-I	UWMgs5a	0.105	11.01	1.50	0.21	-9.47	0.30	10.70	0.010	2.379	0.20	-2.60	0.20
S22	10	Type-I	UWMgs5b	0.105	11.01	2.06	0.14	-8.92	0.26	11.26	0.006	2.384	0.40	-2.50	0.40
S22	10	Type-I	UWMgs6	0.134	10.94	2.49	0.10	-8.50	0.25	11.69	0.009	2.440	0.20	-2.20	0.20
S22	10	Type-I	UWMgs7	0.295	16.61	9.14	0.37	-7.26	0.46	12.96	0.011	2.752	0.20	-1.70	0.20
S22	10	Type-I	UWSd2	0.530	15.88	6.41	0.15	-9.47	0.28	10.71	0.0130	2.995	0.20	-1.40	0.20
S22	10	Type-I	UWSd3	0.645	15.30	5.22	0.04	-10.02	0.23	10.14	0.020	3.110	0.30	-1.50	0.30
S22	10	Type-I	UWSd4	0.938	9.14	0.46	0.37	-8.65	0.44	11.54	0.013	2.983	0.30	-3.20	0.30
S22	10	Type-I	UWSd5	0.797	10.48	-0.26	0.25	-10.72	0.34	9.43	0.015	3.062	0.40	-2.20	0.40
S22	10	Type-I	UWSd1 ^k	0.997	7.92	-0.10	0.12	-8.05	0.25	12.15	0.006	2.946	0.20	-3.50	0.20
S22	10	Type-I	lvig- Sd ^l	0.998	7.79	-	-	-	-	-	-	-	-	-	-
S24	3	Type-II	Brazil Mgs ^h	0.004	15.01	-	-	-	-	-	-	-	-	-	-
S24	3	Type-II	UWMgs1	0.002	12.28	-24.21	0.65	-36.05	0.65	0.00	0.010	1.423	0.74	-1.48	0.74
S24	3	Type-II	UWMgs2	0.012	16.99	-16.75	0.61	-33.18	1.10	2.61	0.017	1.520	0.63	-0.22	0.63
S24	3	Type-II	UWMgs3	0.017	10.58	-	-	-	-	-	-	-	-	-	-
S24	3	Type-II	UWMgs4	0.104	12.62	-11.29	0.15	-23.61	0.93	12.53	0.006	1.865	0.55	-1.08	0.55
S24	3	Type-II	UWMgs5a	0.105	11.01	-13.40	0.45	-24.14	1.01	12.47	0.065	1.836	0.60	-1.41	0.60
S24	3	Type-II	UWMgs5b	0.105	11.01	-	-	-	-	-	-	-	-	-	-
S24	3	Type-II	UWMgs6	0.134	10.94	-	-	-	-	-	-	-	-	-	-
S24	3	Type-II	UWMgs7	0.295	16.61	-3.55	0.83	-19.83	1.18	16.23	0.081	2.578	0.31	0.10	0.31
S24	3	Type-II	UWSd2	0.530	15.88	-4.40	0.38	-19.96	0.75	16.69	0.081	2.658	0.56	0.60	0.56
S24	3	Type-II	UWSd3	0.645	15.30	-5.10	0.42	-20.10	0.77	16.55	0.074	2.796	0.48	-0.06	0.48
S24	3	Type-II	UWSd4	0.938	9.14	-11.23	0.62	-20.19	1.09	16.57	0.053	2.862	0.53	-1.10	0.53
S24	3	Type-II	UWSd5	0.797	10.48	-10.30	0.64	-20.56	1.12	15.69	0.115	2.836	0.43	0.52	0.43
S24	3	Type-II	UWSd1 ^k	0.997	7.92	-12.51	0.25	-20.27	0.88	15.78	0.018	2.773	0.49	-1.08	0.49

Table 3 (continued). SIMS $\delta^{18}\text{O}$ bias data for magnetite-siderite calibration RMs of this study, measured during multiple measurement sessions over a 2-year period (2015–2017)

Session ID	Spot size (μm)	Trend type	RM ID	Fe# ^a	$\delta^{18}\text{O}$ True ^b (%o, VSMOW)	$\delta^{18}\text{O}$ raw ^c	2SE	$\delta^{18}\text{O}$ bias ^{c,d}	2SE	$\delta^{18}\text{O}$ bias*(RM-UWMgs1) ^e	Yield (Gcps/nA)	2SE	$\Delta^{18}\text{O}$ ($\epsilon_F - \epsilon_I$) ^f	2SE
S24	3	Type-II	lvig, Sd ^l	0.998	7.79	—	—	—	—	—	—	—	—	—
S26	3	Type-I	Brazil Mgs ^h	0.004	15.01	—	—	—	—	—	—	—	—	—
S26	3	Type-I	UWMgs1	0.002	12.28	-22.66	0.48	-34.52	0.48	0.00	1.664	0.008	-4.62	0.75
S26	3	Type-I	UWMgs2	0.012	16.99	-15.35	0.43	-31.80	0.43	2.68	1.731	0.021	-4.04	0.59
S26	3	Type-I	UWMgs3	0.017	10.58	-21.19	0.29	-31.44	0.29	3.19	1.690	0.013	-4.07	0.50
S26	3	Type-I	UWMgs4	0.104	12.62	-10.32	0.43	-22.66	0.43	12.14	1.931	0.054	-2.67	0.52
S26	3	Type-I	UWMgs5a	0.105	11.01	-11.74	0.33	-22.50	0.33	12.45	1.895	0.030	-3.64	0.39
S26	3	Type-I	UWMgs5b	0.105	11.01	—	—	—	—	—	—	—	—	—
S26	3	Type-I	UWMgs6	0.134	10.94	-10.79	0.24	-21.49	0.24	13.54	2.070	0.028	-1.94	0.32
S26	3	Type-I	UWMgs7	0.295	16.61	-3.41	0.49	-19.70	0.49	15.19	2.465	0.026	-1.88	0.26
S26	3	Type-I	UWSd2	0.530	15.88	-6.35	0.13	-21.88	0.13	13.09	2.785	0.054	-2.31	0.53
S26	3	Type-I	UWSd3	0.645	15.30	-6.99	0.31	-21.95	0.31	12.87	2.890	0.043	-2.57	0.42
S26	3	Type-I	UWSd4	0.938	9.14	—	—	—	—	—	—	—	—	—
S26	3	Type-I	UWSd5 ⁱ	0.797	10.48	-13.03	0.41	-23.27	0.41	11.71	2.775	0.051	-0.72	0.47
S26	3	Type-I	UWSd1 ^k	0.997	7.92	-14.58	0.34	-22.33	0.34	12.63	2.618	0.027	-2.96	0.46
S26	3	Type-I	lvig, Sd ^l	0.998	7.79	—	—	—	—	—	—	—	—	—

^a Fe# = molar Fe/(Mg + Fe); the uncertainties that accompany this EPMA-derived parameter are tabulated in Table 2.

^b $\delta^{18}\text{O}$ VSMOW value determined by conventional phosphoric acid digestion and gas-source mass spectrometry (see Appendix S1).

^c Value corrected for instrumental drift relative to UWC-3 Reference Bracket.

^d Value calculated via Equations 1 and 3.

^e Value calculated via Equation 4.

^f Cumulative change in $\delta^{18}\text{O}_{\text{raw}}$ between the initial and final cycle of analysis.

^g Calibration data from this session were normalised to the Brazil Mgs end-member rather than to UWMgs1, which was not yet developed at this stage.

^h RM from Eiler *et al.* (1997a). $\delta^{18}\text{O}$ VSMOW value recalculated using phosphoric acid-fractionation factor of Rosenbaum and Sheppard (1986).

ⁱ RM from Eiler *et al.* (1997a).

^j The RM UWSd5 is a new split of JE-Mg-Sid of Eiler *et al.* (1997a).

^k The RM UWSd1 is a new split of lvig, Sd of Eiler *et al.* (1997a) (grains of new split are not rimmed by an FeO coating).

Table 4.
SIMS $\delta^{13}\text{C}$ bias data for magnesite–siderite calibration RMs of this study, measured during multiple measurement sessions over a 2-year period (2015–2017)

Session ID	Spot size (μm)	Trend type	RM ID	Fe# ^a	$\delta^{13}\text{C}$ True ^b (%o, VPDB)	$\delta^{13}\text{C}$ raw ^c	2SE	$\delta^{13}\text{C}$ bias ^{c,d}	2SE	$\delta^{13}\text{C}$ bias* (RM-UWMs1) ^e	2SE	^{12}C Yield (Mcps/nA)	2SE	$\Delta^{13}\text{C}$ ($c_f - c_i$) ^f	2SE
S17 ^g	6	Type-II	Brazil Mgs ^h	0.004	-0.96	-54.71	0.06	-53.80	0.06	0.00	0.34	7.846	0.030	-3.17	1.30
S17 ^g	6	Type-II	UWMs1	0.002	-0.82	-	-	-	-	-	-	-	-	-	-
S17 ^g	6	Type-II	UWMs2	0.012	-5.03	-	-	-	-	-	-	-	-	-	-
S17 ^g	6	Type-II	UWMs3	0.017	-0.32	-	-	-	-	-	-	-	-	-	-
S17 ^g	6	Type-II	UWMs4	0.104	-11.97	-	-	-	-	-	-	-	-	-	-
S17 ^g	6	Type-II	UWMs5a	0.105	-4.92	-	-	-	-	-	-	-	-	-	-
S17 ^g	6	Type-II	UWMs5b	0.105	-4.90	-	-	-	-	-	-	-	-	-	-
S17 ^g	6	Type-II	UWMs6	0.134	-4.95	-61.64	0.21	-55.90	0.21	-2.22	0.44	10.768	0.068	-3.82	0.85
S17 ^g	6	Type-II	UWMs7	0.295	1.35	-	-	-	-	-	-	-	-	-	-
S17 ^g	6	Type-II	UW5d2	0.530	-4.03	-	-	-	-	-	-	-	-	-	-
S17 ^g	6	Type-II	UW5d3	0.645	-5.06	-66.59	0.20	-60.09	0.20	-6.65	0.59	11.497	0.051	-0.74	0.74
S17 ^g	6	Type-II	UW5d4	0.938	-5.49	-	-	-	-	-	-	-	-	-	-
S17 ^g	6	Type-II	UW5d5 ⁱ	0.797	-7.28	-	-	-	-	-	-	-	-	-	-
S17 ^g	6	Type-II	UW5d1 ⁱ	0.997	-8.07	-	-	-	-	-	-	-	-	-	-
S17 ^g	6	Type-II	kg, Sd ^k	0.998	-8.18	-70.90	0.29	-63.24	0.29	-9.97	0.45	8.086	0.056	-3.11	1.36
S18 ^g	6	Type-II	Brazil Mgs ^h	0.004	-0.96	-54.96	0.10	-54.05	0.10	0.00	0.18	9.216	0.114	-2.96	1.26
S18 ^g	6	Type-II	UWMs1	0.002	-0.82	-	-	-	-	-	-	-	-	-	-
S18 ^g	6	Type-II	UWMs2	0.012	-5.03	-	-	-	-	-	-	-	-	-	-
S18 ^g	6	Type-II	UWMs3	0.017	-0.32	-	-	-	-	-	-	-	-	-	-
S18 ^g	6	Type-II	UWMs4	0.104	-11.97	-	-	-	-	-	-	-	-	-	-
S18 ^g	6	Type-II	UWMs5a	0.105	-4.92	-	-	-	-	-	-	-	-	-	-
S18 ^g	6	Type-II	UWMs5b	0.105	-4.90	-	-	-	-	-	-	-	-	-	-
S18 ^g	6	Type-II	UWMs6	0.134	-4.95	-60.72	0.25	-55.61	0.25	-1.64	0.34	11.368	0.128	-4.84	1.06
S18 ^g	6	Type-II	UWMs7	0.295	1.35	-	-	-	-	-	-	-	-	-	-
S18 ^g	6	Type-II	UW5d2	0.530	-4.03	-64.21	0.10	-60.07	0.10	-6.36	0.26	12.867	0.040	-4.49	0.66
S18 ^g	6	Type-II	UW5d3	0.645	-5.06	-66.32	0.16	-61.16	0.16	-7.52	0.30	12.424	0.064	-3.82	0.77
S18 ^g	6	Type-II	UW5d4	0.938	-5.49	-67.10	0.19	-61.88	0.19	-8.28	0.30	9.077	0.147	-4.44	0.71
S18 ^g	6	Type-II	UW5d5 ⁱ	0.797	-7.28	-	-	-	-	-	-	-	-	-	-
S18 ^g	6	Type-II	UW5d1 ⁱ	0.997	-8.07	-	-	-	-	-	-	-	-	-	-
S18 ^g	6	Type-II	kg, Sd ^k	0.998	-8.18	-70.60	0.45	-62.93	0.45	-9.39	0.49	7.984	0.078	-4.10	1.50
S20	6	Type-I	Brazil Mgs ^h	0.004	-0.96	-	-	-	-	-	-	-	-	-	-
S20	6	Type-I	UWMs1	0.002	-0.82	-50.77	0.19	-49.99	0.19	0.00	0.27	7.311	0.029	-2.63	0.84
S20	6	Type-I	UWMs2	0.012	-5.03	-55.71	0.20	-50.26	0.20	-0.28	0.35	7.565	0.062	-2.85	0.60
S20	6	Type-I	UWMs3	0.017	-0.32	-51.03	0.22	-50.46	0.22	-0.49	0.39	8.508	0.581	-2.95	0.56
S20	6	Type-I	UWMs4	0.104	-11.97	-64.42	0.22	-52.59	0.22	-2.74	0.37	9.464	0.063	-3.21	0.89
S20	6	Type-I	UWMs5a	0.105	-4.92	-57.74	0.20	-52.45	0.20	-2.59	0.39	9.531	0.057	-3.42	0.83

Table 4 (continued).
SIMS $\delta^{13}\text{C}$ bias data for magnesite-siderite calibration RMs of this study, measured during multiple measurement sessions over a 2-year period
(2015–2017)

Session ID	Spot size (μm)	Trend type	RM ID	Fe# ^a	$\delta^{13}\text{C}$ True ^b (%o, VPDB)	$\delta^{13}\text{C}$ raw ^c	2SE	$\delta^{13}\text{C}$ bias ^{c,d}	2SE	$\delta^{13}\text{C}$ bias* (RM-UWMgs1) ^e	2SE	^{12}C Yield (Mcps/nA)	2SE	$\Delta^{13}\text{C}$ (r-r-c) ^f	2SE
S20	6	Type-I	UWMgs5b	0.105	-4.90	-	-	-52.65	0.46	-2.80	0.58	10.331	0.040	-3.75	1.23
S20	6	Type-I	UWMgs6	0.134	-4.95	-58.58	0.46	-52.65	0.46	-2.80	0.58	10.331	0.040	-3.75	1.23
S20	6	Type-I	UWMgs7	0.295	1.35	-	-	-	-	-	-	-	-	-	-
S20	6	Type-I	UW5d2	0.530	-4.03	-60.62	0.53	-56.40	0.53	-6.74	0.62	11.341	0.132	-1.74	1.11
S20	6	Type-I	UW5d3	0.645	-5.06	-62.57	0.36	-57.38	0.36	-7.78	0.48	10.974	0.077	-0.90	1.16
S20	6	Type-I	UW5d4	0.938	-5.49	-63.88	0.27	-58.29	0.27	-8.73	0.43	9.224	0.338	-2.05	1.47
S20	6	Type-I	UW5d5 ⁱ	0.797	-7.28	-65.14	0.21	-58.06	0.21	-8.49	0.37	10.215	0.091	-0.88	1.17
S20	6	Type-I	UW5d1 ⁱ	0.997	-8.07	-67.99	0.13	-59.80	0.13	-10.33	0.35	8.264	0.020	-3.72	1.00
S20	6	Type-I	Irig. Sd ^k	0.998	-8.18	-	-	-	-	-	-	-	-	-	-
S23	6	Type-I	Brazil Mgs ^h	0.004	-0.96	-	-	-	-	-	-	-	-	-	-
S23	6	Type-I	UWMgs1	0.002	-0.82	-52.25	0.40	-51.47	0.40	0.00	0.43	8.092	0.118	-4.32	1.19
S23	6	Type-I	UWMgs2	0.012	-5.03	-57.18	0.19	-52.35	0.19	-0.92	0.53	8.554	0.095	-3.72	1.02
S23	6	Type-I	UWMgs3	0.017	-0.32	-52.71	0.22	-52.34	0.22	-0.92	0.54	8.610	0.493	-3.72	2.84
S23	6	Type-I	UWMgs4	0.104	-11.97	-65.72	0.35	-54.40	0.35	-3.08	0.56	10.796	0.101	-4.24	0.91
S23	6	Type-I	UWMgs5a	0.105	-4.92	-58.78	0.44	-54.06	0.44	-2.73	0.66	10.791	0.108	-4.16	1.05
S23	6	Type-I	UWMgs5b	0.105	-4.90	-	-	-	-	-	-	-	-	-	-
S23	6	Type-I	UWMgs6	0.134	-4.95	-59.74	0.28	-55.00	0.28	-3.72	0.56	11.174	0.012	-4.13	1.41
S23	6	Type-I	UWMgs7	0.295	1.35	-54.90	0.21	-56.64	0.21	-5.44	0.51	12.425	0.057	-2.83	0.62
S23	6	Type-I	UW5d2	0.530	-4.03	-62.22	0.23	-58.26	0.23	-7.15	0.53	12.570	0.096	-2.51	0.91
S23	6	Type-I	UW5d3	0.645	-5.06	-63.57	0.31	-58.64	0.31	-7.55	0.57	12.170	0.107	-1.32	1.49
S23	6	Type-I	UW5d4	0.938	-5.49	-65.91	0.34	-60.69	0.34	-9.72	0.59	9.617	0.206	-2.54	1.21
S23	6	Type-I	UW5d5 ⁱ	0.797	-7.28	-67.02	0.50	-60.01	0.50	-9.00	0.69	10.968	0.157	-3.12	1.12
S23	6	Type-I	UW5d1 ⁱ	0.997	-8.07	-69.00	0.31	-61.43	0.31	-10.49	0.53	8.399	0.038	-3.90	1.09
S23	6	Type-I	Irig. Sd ^k	0.998	-8.18	-	-	-	-	-	-	-	-	-	-

^a Fe# = molar Fe/(Mg + Fe); the uncertainties that accompany this EPMA-derived parameter are tabulated in Table 2.
^b $\delta^{13}\text{C}$ VPDB value determined by conventional phosphoric acid digestion and gas-source mass spectrometry (see Appendix S1).

^c Value corrected for instrumental drift relative to UWC-3 Reference Bracket.

^d Value calculated via Equations 2 and 3.

^e Value calculated via Equation 4.

^f Cumulative change in $\delta^{13}\text{C}_{\text{raw}}$ between the initial and final cycle of analysis.

^g Calibration data from this session were normalised to the Brazil Mgs end-member rather than to UWMgs1, which was not yet developed at this stage.

^h RM from Eiler et al. (1997a).

ⁱ The RM UW5d5 is a new split of JE-Mg-Sid of Eiler et al. (1997a).

^j The RM UW5d1 is a new split of Irig. Sd of Eiler et al. (1997a) (grains of new split are not rimmed by an FeO coating).

^k RM from Eiler et al. (1997a).

summaries in Tables 3 and 4). The behaviour of $\delta^{18}\text{O}$ bias calibrations fell into one of two categories: the first consists of trends with two inflection points at constant positions along the compositional axis (Type-I' calibrations; data from three 10- μm spot-size sessions and one 3- μm session) and the second of trends with only one inflection point (Type-II; data from one 10- μm spot-size session and one 3- μm session). The behaviour of $\delta^{13}\text{C}$ bias calibrations also fell into one of two categories of trends with no inflection points: those resembling the general shape of a 3rd-order polynomial (Type-I), and those that could be adequately regressed using a 2nd-order polynomial (Type-II). Two of four sessions represent each type of $\delta^{13}\text{C}$ bias calibration.

Shown in the main body of this work are $\delta^{18}\text{O}$ - and $\delta^{13}\text{C}$ -bias calibrations constructed using measurements from a single mount containing the full suite of RMs (data from sessions: S23 (6- μm $\delta^{13}\text{C}$), S22 (10- μm $\delta^{18}\text{O}$) and two 3- μm $\delta^{18}\text{O}$ sessions – S24 and S26). Shown also, including in Appendix S4, are additional examples of calibrations from earlier (intermediate) stages of development during which time the suite of RMs was distributed among multiple grain mounts (each containing up to twenty grains of five different test materials; see Table SA4-1 for details). These additional examples are included here to demonstrate that the two $\delta^{18}\text{O}$ bias trend types we discuss have been reproducible. Any mount-specific differences in bias measured from any one RM are expected to be $< 0.5\%$. Consider, for example, the data set from session S19 (Appendix S4), where four different mounts were used in building the magnesite–siderite calibration. For any one mount, the average $\delta^{18}\text{O}$ bias value of the co-mounted drift-monitoring material (calcite 'UWC-3'; Kozdon *et al.* 2009) differs by $< 0.5\%$ relative to all other mounts. Thus, any potential mount-to-mount bias differences do not provide a tenable explanation for the existence (at present) of two different $\delta^{18}\text{O}$ and $\delta^{13}\text{C}$ trend types. Note in particular that both types of $\delta^{18}\text{O}$ bias behaviour have been observed on separate occasions using the same set of grains on a single calibration mount using the same 3- μm spot-size $\delta^{18}\text{O}$ configuration (Appendix S4: Table SA4-1).

The behaviour of SIMS $\delta^{18}\text{O}$ bias along the magnesite–siderite binary

In all instances (Type-I and II trends), the change in the $\delta^{18}\text{O}$ bias (un-normalised) between the end-members of the magnesite–siderite solid-solution series was not unidirectional. To a first-order, however, the magnitude of the bias decreased as a function of increasing Fe content (Figure 2a, b). In other words, the per mil difference between $\delta^{18}\text{O}_{\text{RM}}$ as measured by SIMS and the 'accepted' $\delta^{18}\text{O}_{\text{VSMOW}}$ values

became smaller. The bias was always largest for end-member magnesite (ca. -20 to -25% with 10- μm spot-size and -35% with 3- μm spot) and different by 12–16% in relation to end-member siderite (approximately -8 to -12% with 10- μm spot and -20% with 3- μm spot). From here on the discussion will focus on *working calibration curves* (Figure 2c, d), for which $\delta^{18}\text{O}$ bias values were normalised to the RM with $\text{Fe}\# = 0.0$ (i.e., values expressed as $\delta^{18}\text{O}$ bias*(RM-UWMgs1)), and thus are seen to increase with $\text{Fe}\#$.

Type-I $\delta^{18}\text{O}$ trends: 10- μm spot-size set-up (3 sessions): The more common Type-I $\delta^{18}\text{O}$ calibrations can be described as follows. A representative trend is shown in Figure 2c (session S22 data). The magnitude of SIMS $\delta^{18}\text{O}$ bias*(RM-UWMgs1) increased exponentially by $\sim 13.5\%$ between $\text{Fe}\# = 0.0$ and the first inflection point at $\text{Fe}\# = 0.25$. This was followed by a gradual decrease of $\sim 4\%$ out to the second inflection point at $\text{Fe}\# = 0.7$, and lastly an upward rebound of $\sim 2.5\%$ between $\text{Fe}\# = 0.7$ and 1.0. The calibration data were regressed using the following mathematical expression, which stems from the probabilistic properties of the same Hill function (e.g., Hill 1910, Goutelle *et al.* 2008) used in recent work on $\delta^{18}\text{O}$ and $\delta^{13}\text{C}$ matrix effects in the dolomite–ankerite series (Śliwiński *et al.* 2016a, b). Hill-type equations are well-suited for describing empirical relationships between the intensity of a measured effect (or response) and the concentration of a certain component(s) in the system under observation, especially in the case of systems that behave non-linearly and reach saturation:

$$\text{bias}^*(\text{RM} - \text{UWMgs1}) = C_1 \left(\frac{nx^{n-1}}{k^n + x^n} \right) + C_2 x^d + C_3 \quad (6)$$

With the addition of the x^d term along with the three constants ' C_1 ', ' C_2 ' and ' C_3 ', this is a modified form of equation 27 of Goutelle *et al.* (2008), where ' n ', ' k ' and ' d ' are curve-shape parameters and ' x ' in our application is the $\text{Fe}\#$ of either a sample or RM. The influence of the shape parameters on the regression is shown graphically in Appendix S4: Figure SA4-1, along with a step-by-step graphical description of the trend-fitting process. The constants ' C_1 ' and ' C_2 ' allow for vertical stretching/compression of the working calibration curve (Figure 2c, session S22 trend) to account for the fact that measured bias values can differ by up to several ‰ on a session-to-session basis (a new session is defined any time significant changes are made in tuning parameters; typically a session lasts from 2–5 days). Lastly, the constant ' C_3 ' accounts for the fact that the calibration curves would not be anchored to the origin (0,0) if an RM other than UWMgs1 were used as the normaliser

(thus in the present case ' C_3 ' = 0). This becomes relevant when one attempts to fit a surface model to bias data for the entire Ca-Mg-Fe carbonate ternary. For this, it is necessary to normalise the bias of all carbonate RMs (i.e., calcites, dolomite–ankerites, magnesite–siderites) to a common 'anchor'. Consider, for example, setting dolomite rather than magnesite as the common normaliser (i.e., the (0,0) point). Doing so would have the effect of offsetting the regression of the magnesite–siderite series by the magnitude of the bias difference between the two RMs (i.e., $\delta^{18}\text{O}$ bias* (dolomite_{end-member} – magnesite_{end-member})) but would have no effect on the overall shape of the calibration curve. Because ' C_3 ' is simply a ratio of two measured values, it does not need to be determined by a fitting algorithm, leaving Equation (6) an empirical expression of five parameters.

Regressing the oxygen isotope bias data from the full suite of calibration RMs (Figure 2c, session S22) yields the following curve-shape parameter (n,k,d) and constant (C_1, C_2) values (\pm 2SE): $n = 1.8$ (\pm 0.1), $k = 0.26$ (\pm 0.04), $d = 4.2$ (\pm 2.9), $C_1 = 3.8$ (\pm 1.0) and $C_2 = 5.9$ (\pm 1.2), and $C_3 = 0$. This same set of curve-shape parameter values was successfully applied in regressing calibration data from two earlier sessions during which fewer RMs were available (Appendix S4: Figure SA4-2). In all three instances, the measured average value of $\delta^{18}\text{O}$ bias*(RM-UWMgs1) for all RMs differs by less than 0.5‰ from the output of the calibration model (see residual plots in Figures 2c and Appendix S4: Figure SA4-2). This can be considered a measure of accuracy in relation to CRM NIST-19 (Verkouteren and Klinedinst 2004). The calibration residual shows no significant correlation to the minor Ca content of some of these materials ($r = 0.04$; up to 1.07 mol% CaCO_3 end-member), or to the more substantial Mn concentrations ($r = 0.19$; up to 8.35 mol% MnCO_3 end-member). No secondary matrix corrections were thus required for this particular suite of RMs.

Including Mn in the Fe# calculation, on account of its appreciable concentration in the RM suite and the overall similarity of Mn^{2+} to Fe^{2+} in terms of mass and ionic radius, neither significantly improved nor degraded the quality of the regression (see Appendix S4: Figure SA4-3). Note, however, that the most Mn-enriched RMs in the suite do not fall near the magnesite end-member of the solid-solution series, where $\delta^{18}\text{O}$ bias changes most rapidly as a function of cation chemistry. It is likely for this reason that the regression remains unaffected. In the hypothetical case of samples that are enriched in Mn but deficient in Fe, it may be advisable to plot bias as a function of (Fe + Mn)# (i.e., molar (Fe + Mn)/(Mg + Fe + Mn)), although future studies will need to resolve more conclusively how the effects of Mn-

substitution on $\delta^{18}\text{O}$ bias in both the magnesite–siderite and dolomite–ankerite series compare with those of iron.

3- μm spot-size set-up (1 session): A different set of routine analytical conditions is used at WiscSIMS for 3- vs. 10- μm spot carbonate $\delta^{18}\text{O}$ analyses (described in Śliwiński *et al.* 2016a). Notably, the small 3- μm spot-size configuration makes use of a weaker primary Cs^+ ion beam (600 pA vs. 1.2 nA) and employs an electron multiplier for detecting the minor isotope ($^{18}\text{O}^-$) in the secondary ion stream (as opposed to a Faraday cup). One of the two 3- μm calibrations generated to date strongly resembled the three self-consistent 10- μm trends (Figure 2d, session S26 data; compare with session S22 trend in Figure 2c) and was successfully modelled using the same empirical expression (Eqn. 6), yielding residuals \leq 0.5‰ (Figure 2d) and the following parameter values (\pm 2SE): $n = 1.9$ (\pm 0.1), $k = 0.24$ (\pm 0.06), $d = 1.6$ (\pm 1.9), $C_1 = 3.9$ (\pm 1.8) and $C_2 = 5.8$ (\pm 2.4), and $C_3 = 0$. Note that the values of the curve-shape parameters n and k and the constants C_1 and C_2 are within 2SE limits of those associated with the 10- μm trends.

This 3- μm trend differs from the above mentioned 10- μm calibrations in that the magnitude of SIMS $\delta^{18}\text{O}$ bias*(RM-UWMgs1) increased markedly by \sim 15.5‰ (i.e., by an additional 2‰ compared with the 10- μm trends) between Fe# = 0.0 and the first inflection point at Fe# = 0.25. At the present time, however, this should not be viewed as a general conclusion about differences between 3- and 10- μm calibrations. The number of data sets is still limited, and this 2‰ difference in the magnitude of the maximum bias between the end-members of a solid-solution falls within the general range of expected session-to-session variability (compare with Śliwiński *et al.* 2016a, b). A potentially more meaningful difference may lie in the observation that the bias maximum (relative to UWMgs1) at Fe# = 0.25 is followed by a more gradual decrease of \sim 3‰ out to the second inflection point at Fe# = 0.7 and the disappearance of a significant rebound between Fe# = 0.7 and 1.0 (compared with 10- μm trends).

Type-II $\delta^{18}\text{O}$ trends: 10- μm and 3- μm spot-size set-ups: The alternative behaviour of $\delta^{18}\text{O}$ bias calibrations, shown in Figure 2c, d, was observed under both 10- and 3- μm spot-size conditions. These Type-II trends represent two of the six sessions to date. The behaviour was as follows. Starting at Fe# = 0.0, the magnitude of SIMS $\delta^{18}\text{O}$ bias*(RM-UWMgs1) in both instances increased exponentially and reached a maximum of \sim 16.5‰ around Fe# = 0.4–0.5. Values then steadily declined by 1–2‰ out to

Fe# = 1.0. This behaviour was modelled by combining the Hill equation (in the form used to model bias in the dolomite–ankerite series; Equation (5) herein) and the second term of Equation (6), which allows the Hill function to descend after reaching a maximum value:

$$\text{bias}^*(\text{RM} - \text{UWMgs1}) = \left(\frac{\text{Bias}_{\text{max}}^* x^n}{k^n + x^n} \right) + C_2 x^d \quad (7)$$

All terms are as defined earlier.

Assessment of potential crystallographic orientation effects on $\delta^{18}\text{O}$ bias

To our knowledge, crystallographic orientation effects on $\delta^{18}\text{O}$ bias (analogous to those described by Huberty *et al.* 2010, Kita *et al.* 2011) have not yet been investigated for carbonates of the magnesite–siderite series. We performed a simple test using two different mounts, each containing grains of siderite (RM UWSd1) and two of ferroan magnesite (RMs UWMgs4 and 5a) exposed at the analytical surface in one of two broadly different sets of orientations with respect to the primary and secondary ion beams.

The first category of orientations includes those where the rhombic cleavage of magnesite and siderite grains is parallel to subparallel with regard to the flattened and polished analytical surface of the 1-inch diameter epoxy mount; these orientations tend to be over-represented when laying out grains on casting plates, although the variable rotational positioning of cleavage faces does diversify the number of unique crystallographic orientations that will eventually be exposed for measurement. It does not, however, allow for an assessment of whether $\delta^{18}\text{O}$ bias differs significantly along the crystallographic planes that are normal to subnormal to: (a) rhomb edges or to the (b) rhomb body-diagonal long axis. These orientations

comprise the second category. A grain mount was prepared with only this second category of orientations exposed by supporting grains during casting with strips of ridged carbon tape arranged in a series of parallel trenches ~ 0.5 mm deep and spaced ~ 0.5 mm apart (Appendix S4: Figure SA4-4).

Measurements of $\delta^{18}\text{O}$ bias from both mounts were performed on the same day of analysis (session S21) and were found to be well within the $\pm 0.3\%$ 2s repeatability of the UWC-3 bracketing RM used to monitor instrument drift (Table 5). In other words, there is no significant difference in bias between the two broad categories of crystallographic orientations described above.

Current insights and future directions towards understanding the complexities of $\delta^{18}\text{O}$ bias trends for the magnesite–siderite series

The $\delta^{18}\text{O}$ bias response of carbonate compositions between Fe# 0.0 and 0.3 is comparable for Type-I and -II calibrations under both 3- and 10- μm spot-size conditions (Figure 2c, d; for ease of comparison, all four trends are co-plotted in Appendix S4: Figure SA4-5). Recall that calibration trends can stretch or contract by up to several per mil along the bias axis from session to session while maintaining constant curve-shape parameter values (and that a session-specific scaling factor relates them; Śliwiński *et al.* 2016a, b). Divergence in trend shape is driven by the session-specific trajectory taken by compositions beyond Fe# 0.5, and has, to date, resulted in bias differences of 2–6‰ for the subset of RMs between Fe# 0.5 and 1.0.

We have focused here primarily on presenting the first detailed descriptions of $\delta^{18}\text{O}$ bias behaviour for carbonates of the magnesite–siderite series, and on outlining a functional calibration scheme. The existence at present of

Table 5.
Results of crystallographic orientation effect test on measured $\delta^{18}\text{O}$ bias

RM ID	Fe#	Grain mount type	$\delta^{18}\text{O}_{\text{raw}}$ (‰)	$\delta^{18}\text{O}$ bias	2s ^a	n
UWSd1	0.997	Regular ^b	-4.56	-12.38	0.26	4
UWSd1	0.997	Oriented ^c	-4.67	-12.49	0.28	8
UWMgs5a	0.105	Regular ^b	-3.86	-14.71	0.58	5
UWMgs5a	0.105	Oriented ^c	-3.90	-14.75	0.72	10
UWMgs4	0.104	Regular ^b	-2.12	-14.56	0.25	4
UWMgs4	0.104	Oriented ^c	-2.13	-14.57	0.29	8

^a Among-grain variability.

^b When grains are laid out on a flat casting plate, the rhombic geometry of carbonate grains results in an under-representation of edges and apices.

^c Mount with grain edges and apices oriented perpendicular to casting plate surface (grains embedded into deep grooves cut into 1-mm thick and stiff carbon tape).

two different $\delta^{18}\text{O}$ calibration trend types – along with the possibility that more variability in trend shape may be encountered with time – does not limit our ability to make accurate bias corrections ($< 0.5\%$ relative to NIST-19), provided that a sufficient number of reference materials – spanning the range of compositions between magnesite and siderite – are available and utilised each session. Understanding the underlying cause(s) of the complexity we encountered with this solid-solution series, however, requires further study and should perhaps serve as a reminder that calibrating SIMS instruments for analysis of geological materials remains entirely empirical in nature.

The findings of this study stand in contrast to our experience with calibrating the dolomite–ankerite series. The Hill equation introduced previously (Śliwiński *et al.* 2016a, b) has been applied over a 3-year period using the same curve-shape parameter values to regress calibration data acquired using the same analytical protocols for 3- and 10- μm spot-size $\delta^{18}\text{O}$ analysis. Why, then, do these two carbonate solid-solutions behave differently under the same analytical conditions? One possibility is that the $\delta^{18}\text{O}$ bias response is insensitive to slight session-specific differences in

instrument tuning below some threshold Fe (+Mn?) concentration. Consider the dolomite–ankerite calibration data compared with that of the magnesite–siderite series shown in Figure 3a (note that composition is expressed here as a molar ratio of Fe+Mn to the sum total of Ca, Mg, Fe and Mn [i.e., $X_{(\text{Fe}+\text{Mn})}$] to account for the fact that Ca ideally occupies one-half of all cation sites in the dolomite structure). The Fe content of the dolomite–ankerite reference material suite does not extend into the compositional field where Type-I and -II $\delta^{18}\text{O}$ bias trends of the magnesite–siderite series diverge in shape (note that the maximum Fe content of naturally occurring ankerites seems to be limited to $X_{(\text{Fe}+\text{Mn})} \approx 0.4$; e.g., Chang *et al.* 1996).

Something of potential interest to note here in moving forward is that certain electromagnetic properties of carbonate minerals vary by several orders of magnitude as a function of Fe + Mn content. One example is electrical resistivity (2×10^{12} vs. 70 $\text{m}\Omega$ for calcite and siderite, respectively; e.g., Telford *et al.* 1990). Another is magnetic susceptibility (MS), which increases by a factor of 100 between dolomite and ankerite, compared with a factor of 1000 between magnesite and siderite (Figure 3b; see e.g.,

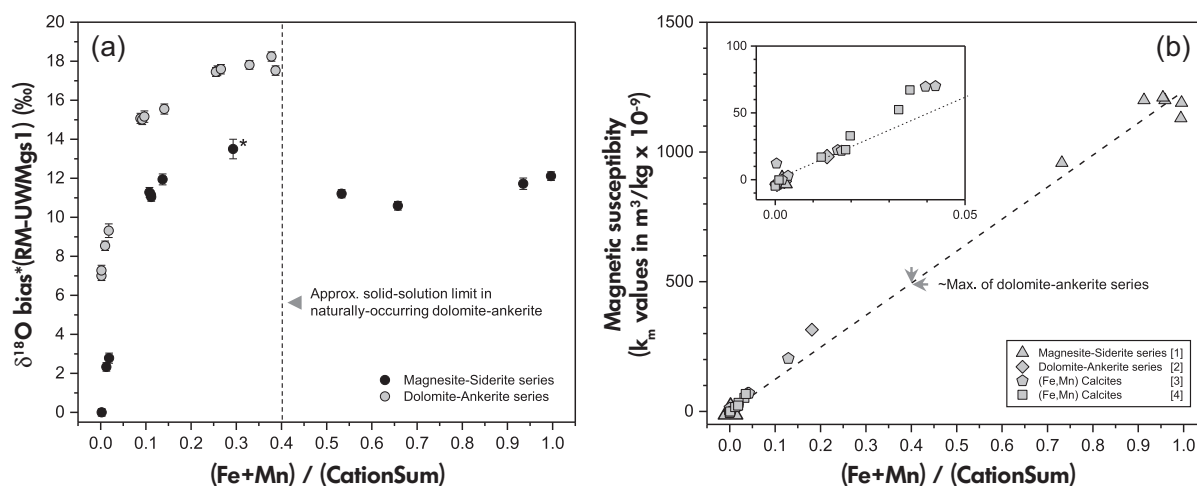


Figure 3. (a) A comparison of SIMS $\delta^{18}\text{O}$ bias measured from carbonates of the dolomite–ankerite and magnesite–siderite solid-solution series using the same conditions during a single analytical session (asterisks indicate a modelled bias value; refer to Figure SA4-2b). Composition is plotted here as a molar ratio of Fe + Mn to the sum of all cations (i.e., $X_{(\text{Fe}+\text{Mn})}$) to facilitate comparison with data in (b), which shows systematic changes in the magnetic susceptibility (MS) of carbonates as a function of Fe + Mn concentration (data from: [1,2] Schmidt *et al.* 2007, [3] Schmidt *et al.* 2006, [4] Rochette 1988). Note that the Fe + Mn content of the dolomite–ankerite RM suite (Śliwiński *et al.* 2016a) does not extend far into the compositional field where Type-I and -II bias trends of the magnesite–siderite series begin to diverge in shape ($X_{(\text{Fe}+\text{Mn})} > \sim 0.3$; see Appendix S4: Figure SA4-5), suggesting that the $\delta^{18}\text{O}$ bias response is insensitive to slight session-specific differences in instrument tuning below this threshold (i.e., differences in trend shape are not expected for the dolomite–ankerite series and indeed have not been observed over the last 3-year period).

Rochette 1988, Hunt *et al.* 1995, Schmidt *et al.* 2006, 2007). We can speculate that properties of this nature make the magnesite–siderite series more sensitive to session-specific differences in tuning of the instrument – which can manifest as differences in pit morphology (Appendix S4: Figures SA4-6 and SA4-7) – by influencing the behaviour of the electron cloud which provides charge compensation during sputtering (and its role in promoting the formation of secondary oxygen ions).

A potentially promising direction for future studies is an assessment of how bias trends differ in shape (if at all) when the spot-size is intentionally made smaller or larger by ~ 25–50% under otherwise routine $\delta^{18}\text{O}$ analysis conditions where the target spot-size is 10- μm , for example. Using a primary beam of the same intensity and a fixed analysis time, this would necessarily force a change in the pit depth for a given carbonate composition (to maintain a constant volume of sputtered material). A natural extension of such experiments would be a rigorous assessment of sputtering rates for the different common Ca-Mg-Fe carbonate minerals. In light of analogous studies in silicate systems (e.g., Eiler *et al.* 1997b, Isa *et al.* 2017), this could significantly improve our understanding of what drives the first-order differences of ~ 10–20‰ in bias magnitude between the end-members of the dolomite–ankerite and magnesite–siderite solid-solution series.

We next continue our discussion of $\delta^{18}\text{O}$ matrix effects by briefly examining how some of the base signals associated with Type-I and -II calibration trends differ as a function of RM composition. We evaluated how Fe# affects $^{16}\text{O}^-$ ion yields and the magnitude of drift in the raw isotope ratio over the course of a single spot analysis. This provides further insight into the circumstances under which inflection points appear in calibration curves, and may be of use in designing further experimental studies seeking to suppress this complexity. No comprehensive model based on first principles exists at present for accurately predicting secondary ion yields from geological materials (and hence the bias imparted to isotope ratios during sputtering). An important component of developing and testing such models, however, is a clear empirical understanding of how base signals vary as a function of composition for solid-solution mineral series under different analytical conditions (consider, e.g., the work of Riciputi *et al.* 1998).

Dependence of $^{16}\text{O}^-$ ion yield on Fe#: The shape of ion yield vs. Fe# trends responds to session-specific differences in tuning. Under both small- and large-spot conditions, ion yields were always smallest from magnesite and

increased as a function of Fe content out to Fe# = 0.645; from here, yields either continued increasing out to the siderite end-member (Type-II trends) or began a gradual decline (Type-I trends; 5 to 10% decrease relative to the maximum value at Fe# 0.645 under large- and small-spot conditions, respectively). In more detail:

Under 10- μm spot-size conditions, ion yield trends associated with Type-I and -II $\delta^{18}\text{O}$ bias calibrations followed different trajectories (parabolic vs. sigmoidal, respectively; see Figure 4a and additional examples in Appendix S4: Figure SA4-8). The ion yields of Type-I trends varied by ~ 1 Gcps nA^{-1} between the end-members of the solid-solution, whereas the difference associated with the one example of a Type-II trend observed under these conditions was twice as large. Qualitatively, the rate of change in ion yield was similar for both trend types between Fe# 0.105 and 0.645 but differed considerably near the end-member compositions, where the steeper slopes seen in the Type-II trend resulted in a comparatively higher ion yield from siderite (by ~ 0.5 Gcps nA^{-1} , a ~ 15% difference) and a lower yield from magnesite (by ~ 0.3 Gcps nA^{-1} , also a ~ 15% difference).

Under 3- μm spot-size conditions, the ion yield trends associated with both bias calibrations followed parabolic trajectories with maxima at different compositions (at Fe# 0.645 for the Type-I trend and at the siderite end-member for the Type-II trend; Figure 4b). In both cases count rates varied by 1.3 Mcps nA^{-1} . Qualitatively, the rate of change in ion yield was similar between Fe# 0.105 and 0.645; however, a steepening of slope associated with the Type-II trend below Fe# 0.105 (analogous to that observed under large-spot conditions) resulted in a comparatively lower ion yield from magnesite (by ~ 0.3 Gcps nA^{-1} , a change of ~ 14.5%). Because the two trends crest at different compositions, a count rate difference of 0.15 Gcps nA^{-1} (a ~ 6% difference) was observed from the siderite end-member.

Note that in the case of Type-II bias calibrations under both small- and large-spot analysis conditions, the ion yield is a function of Fe# and Fe# is a function of ion yield (Figure 4a and b). Thus, hypothetically, the Fe# of a sample material under the beam could be estimated from its ion yield (and this then fed into a Fe# vs. bias calibration to determine the appropriate matrix correction factor). Whereas this is not the case for Type-I bias calibrations, the very fact that the shape of ion yield vs. Fe# trends responds to session-specific differences in tuning hints at a potential analytical advantage that could be gained through further refinements in technique.

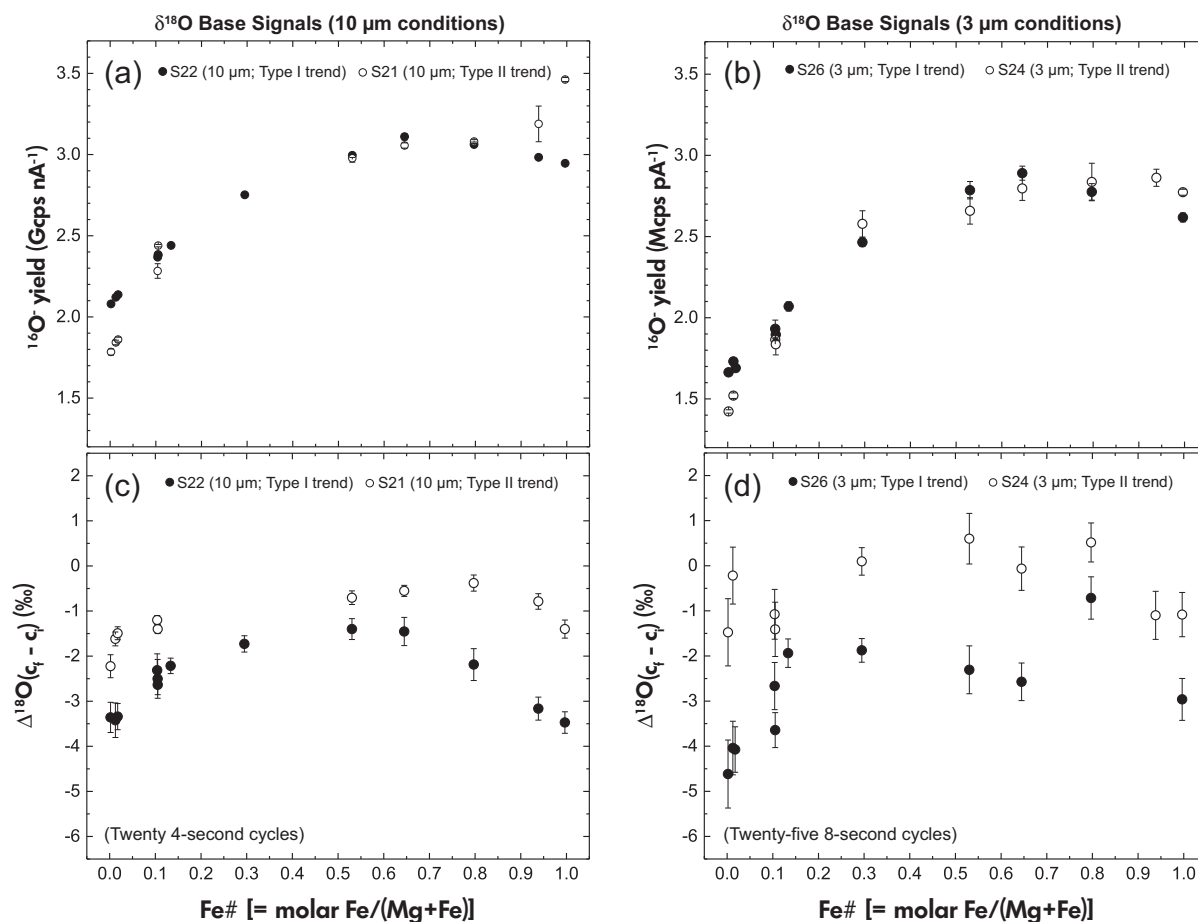


Figure 4. The compositional dependence of certain base signals associated with SIMS $\delta^{18}\text{O}$ bias measurements from the magnesite–siderite series. (a, b) Secondary $^{16}\text{O}^-$ ion yields vs. Fe# and (c, d) the cumulative change in $\delta^{18}\text{O}_{\text{raw}}$ between the initial (*i*) and final (*f*) cycles of analysis (“ $\Delta^{18}\text{O}(c_f - c_i)$ ”) vs. Fe# for both 10- and 3- μm spot-size analysis conditions. Yield = count rate (as mega or giga counts per second) / primary Cs^+ ion beam intensity (pA or nA). Each point is an average of at least four measurements from four separate grains (one analysis/grain). (See text for description of ‘Type-I’ vs. ‘Type-II’ bias trends).

Cumulative change in $\delta^{18}\text{O}_{\text{raw}}$ during sputtering as a function of Fe#: The raw $\delta^{18}\text{O}$ value reported for each analysis spot is an average of multiple data collection cycles (twenty cycles of 4 s each and twenty-five cycles of 8 s under 10- and 3- μm spot-size conditions, respectively). It is thus possible to assess if/how the raw signal changes during sputtering, and if the magnitude of this change is systematically related to composition. Repeat measurements of each RM were therefore summarised on a cycle-by-cycle basis, where all cycle 1 measurements were compiled and averaged, followed by all cycle 2 measurements, etc. Plotting this data shows linear trends towards lower $\delta^{18}\text{O}$ values with each passing cycle under both sets of measurement conditions (i.e., fractionation in favour of the lighter isotope increases with time; see cycle-by-cycle plots in Figures SA4-9 to 4-12). The cumulative change in $\delta^{18}\text{O}_{\text{raw}}$ between the first

and last cycle of analysis (“ $\Delta^{18}\text{O}(c_f - c_i)$ ”) shows a dependence on composition (the terms ‘ c_i ’ and ‘ c_f ’, respectively, refer to the initial and final cycles). In a qualitative sense, the dependence of $\Delta^{18}\text{O}(c_f - c_i)$ on Fe# follows well- to moderately well-defined parabolic trajectories under both large- and small-spot conditions, respectively (Figure 4c, d). Values of $\Delta^{18}\text{O}(c_f - c_i)$ tend to be smallest near the midpoint of the solid-solution (i.e., consider the least negative values in Figure 4c, d, which represent the least amount of down-pit discrimination against ^{18}O). Values of $\Delta^{18}\text{O}(c_f - c_i)$ are largest (i.e., most negative) at the compositional end-members and are of equal to subequal magnitude. If we regard the average $\Delta^{18}\text{O}(c_f - c_i)$ value of the magnesite and siderite end-members as a baseline (as frame of reference), then we note the following: (a) the baseline is lower in the case of Type-I (approximately -

3.5‰) vs. Type-II (approximately -1.5‰) $\delta^{18}\text{O}$ bias calibrations under both large- and small-spot conditions (there is necessarily more scatter in the small-spot data due to comparatively poorer counting statistics); (b) the range of $\Delta^{18}\text{O}(c_f - c_i)$ values is somewhat larger in the case of Type-I (approximately 2‰) vs. Type-II (approximately 1.5‰) $\delta^{18}\text{O}$ bias calibrations under both large- and small-spot conditions (Figure 4c, d).

In comparing the base signals of Type-I and -II calibration trends and in reflecting on how they affect measured bias values, we observe that the lower ion yields associated with the Type-II trend near the magnesite end-member ($\text{Fe}\# < 0.2$) correspond to larger bias values (by up to 6‰; see Figure 2a). This follows general expectations. Surprisingly, however, larger bias values were also observed near the siderite end-member ($\text{Fe}\# > 0.8$; by up to 4‰; Figure 2a) despite ion yields being higher (compared with the Type-I trend). At the same time, the $\Delta^{18}\text{O}(c_f - c_i)$ vs. $\text{Fe}\#$ trends of both $\delta^{18}\text{O}$ calibration types are generally comparable beyond a baseline shift (for each trend, note the similar magnitude of $\Delta^{18}\text{O}(c_f - c_i)$ for the end-members and the general symmetry of the data distributions in Figure 4c). Differences in the topology of Type-I vs. Type-II bias calibrations do not seem to be readily explainable by considering only a simple interplay between these two base variables (i.e., trends in ion yield and $\Delta^{18}\text{O}(c_f - c_i)$ as a function of $\text{Fe}\#$). We suspect that differences in sputtering rate contribute here as well, as a visual comparison of pit images (Appendix S4: Figures SA4-6 and SA4-7) suggests that pit depth (and hence sputtering rate) increases with increasing Fe content. Given what is known from silicate systems, bias and sputtering rate can correlate strongly and non-linearly (e.g., Eiler *et al.* 1997b, Isa *et al.* 2017). Nonetheless, what is apparent from the data at hand is that above a certain threshold Fe mass fraction, carbonate $\delta^{18}\text{O}$ bias calibration curve shapes are strongly influenced by session-specific differences in instrument tuning (reflected by the resulting pit morphologies/geometries). Where tuning conditions accentuate differences in base parameters such as ion yield and the observed down-hole drift of the raw isotope ratio during sputtering, the end result is a more complex calibration curve (compare base signals and corresponding bias curves of Type-I and -II trend in Figures 2 and 4).

The behaviour of SIMS $\delta^{13}\text{C}$ bias along the magnesite–siderite binary

In all instances (Type-I and II trends), the change in the magnitude of $\delta^{13}\text{C}$ bias (un-normalised) between the end-members of the magnesite–siderite solid-solution series is

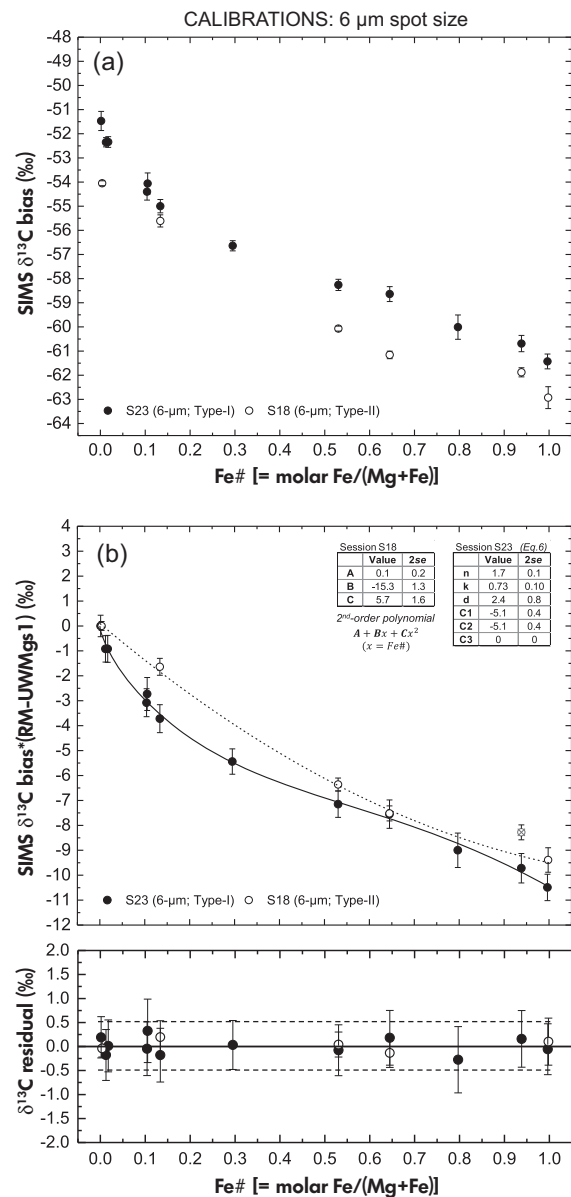


Figure 5. (a) Plot relating SIMS $\delta^{13}\text{C}$ bias (‰) to the cation composition of carbonates belonging to the siderite–magnesite solid-solution series [$\text{Fe}\# = \text{Fe}/(\text{Mg} + \text{Fe})$, molar]. Shown are two types of bias behaviour observed using a consistent analytical protocol for 6- μm diameter spot-size measurements. (b) Working calibration curves based on the data plotted in (a), where bias values are normalised to end-member magnesite (expressed as $\delta^{13}\text{C}$ bias*(RM-UWMgs1)), which serves as the calibration anchor (crossed-circle denotes an outlier). Immediately below are the calibration residuals, which can be considered a measure of accuracy relative to the CRM NIST-19.

consistently unidirectional (albeit non-linear). Relative to the magnesite end-member, the bias *increases* by $\sim 10\text{‰}$ as a function of increasing Fe content (Figure 5a). In other words, the per mil difference between $\delta^{13}\text{C}_{\text{raw}}$ as measured by SIMS and the ‘accepted’ $\delta^{13}\text{C}_{\text{VPDB}}$ values becomes *larger* (as values became more negative, the bias is said to *increase*). The bias is always *smallest* for end-member magnesite (-51.5‰) and different by 10‰ in relation to end-member siderite (approximately -61.5‰) (session S23 data, see also Table 4 and calibrations from other sessions in Appendix S4: Figure SA4-15). From here on the discussion will focus on *working calibration curves* (Figure 5b), for which $\delta^{13}\text{C}$ bias values have been normalised to that of the magnesite end-member anchor (i.e., values expressed as $\delta^{13}\text{C}$ bias*(RM-UWMs1)).

Type-I and II $\delta^{13}\text{C}$ trends: The shape of Type-I $\delta^{13}\text{C}$ calibrations resembles a gently flexing 3rd-order polynomial (Figure 5b; session S23 data). The bias response was most sensitive to changes in cation chemistry in the Fe# range between 0.0 and 0.3 (change of $\sim 5.5\text{‰}$ relative to end-member magnesite). Between Fe# 0.3 and 1.0, the change was more gradual (approximately linear), with $\delta^{13}\text{C}$ bias*(RM-UWMs1) values changing by an additional $\sim 5.5\text{‰}$ over this much broader range of compositions. The data were regressed using Equation (6), yielding the following parameter values (± 2 se): $n = 1.7 (\pm 0.1)$, $k = 0.73 (\pm 0.1)$, $d = 2.4 (\pm 0.8)$, $C_1 = C_2 = -5.1 (\pm 0.4)$ and $C_3 = 0$. This same set of curve-shape parameter values was successfully applied in regressing calibration data from one other session that yielded a Type-I trend (Figure SA4-15). In both instances, the measured average value of $\delta^{13}\text{C}$ bias*(RM-UWMs1) for all RMs differs by $< 0.5\text{‰}$ from the output of the calibration model (see residual plots in Figure 5b and Appendix S4: Figure SA4-15). This can be considered a measure of trueness in relation to CRM NIST-19 (Verkouteren and Klinedinst 2004). As with $\delta^{18}\text{O}$, the calibration residuals show no correlation to calcium ($r = 0.03$) or manganese ($r = 0.15$) content, and the calibration remains unchanged with the inclusion of Mn in the Fe# (Appendix S4: Figure SA4-3). No secondary matrix corrections are thus required for this particular suite of RMs.

In contrast, the shape of Type-II $\delta^{13}\text{C}$ calibrations can be adequately described by gently flexing 2nd-order polynomials, yielding residuals $< 0.5\text{‰}$ (Figure 5b; session S18 data). The change in bias is thus more gradual when compared with Type-I trends but is of the same general magnitude ($\sim 10\text{‰}$) across the entire solid-solution series (one additional example is shown in Appendix S4: Figure SA4-15; please note that both examples of Type-I trends represent sessions from earlier stages research when far

fewer RMs were available). The shape of both trend types differed most in the compositional space between Fe# = 0 and 0.5, where RM bias values changed on a session-by-session basis by up to $1\text{--}2\text{‰}$.

We continue our discussion of $\delta^{13}\text{C}$ matrix effects by briefly examining how base signals varied with RM composition. The ^{12}C ion yields associated with the two different $\delta^{13}\text{C}$ bias calibration trend types shown in Figure 5 are plotted as a function of composition in Figure 6a (see also Appendix S4: Figure SA4-16). The ion yield of the Type-I

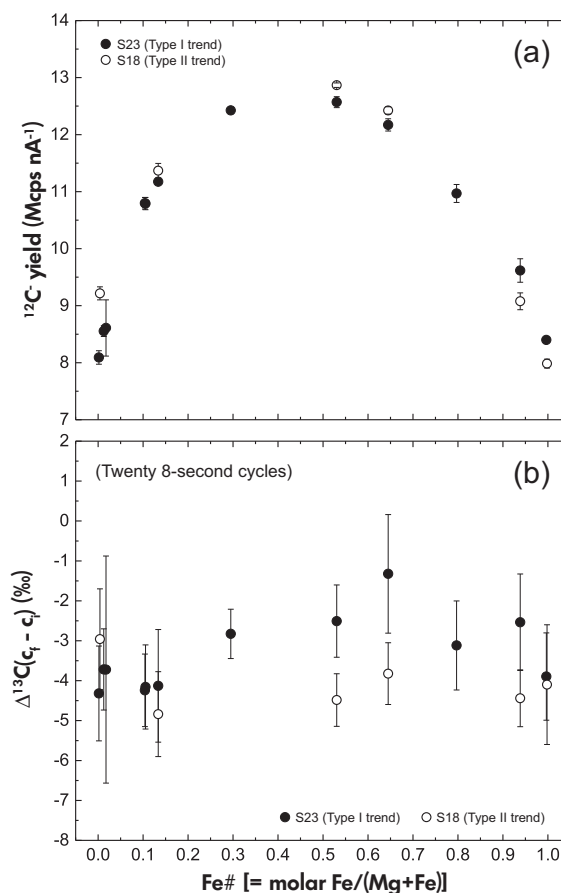


Figure 6. The compositional dependence of certain base signals associated with SIMS $\delta^{13}\text{C}$ bias measurements from the magnesite–siderite series. (a) Secondary ^{12}C ion yields vs. Fe# and (b) the cumulative change in $\delta^{13}\text{C}_{\text{raw}}$ between the initial (*i*) and final (*f*) cycles of analysis (“ $\Delta^{13}\text{C}(c_f - c_i)$ ”) vs. Fe# under $6\text{-}\mu\text{m}$ spot-size analysis conditions. Yield = count rate (as mega counts per second)/primary Cs⁺ ion beam intensity (nA). Each point is an average of at least four measurements from four separate grains (one analysis/grain). (See text for description of ‘Type-I’ vs. ‘Type-II’ bias trends).

trend can be described as a parabolic function of Fe# that is symmetric around the mid-point composition of the solid-solution, where it achieves a maximum value of ~ 12.5 Mcps nA^{-1} . Count rates were lowest and of the same general magnitude from the compositional end-members (~ 8 Mcps nA^{-1}). The ion yield of the Type-II trend also followed a parabolic trajectory with a maximum near the compositional mid-point (~ 13 Mcps nA^{-1}), although the count rates measured from the end-members were dissimilar (~ 9 and 8 Mcps nA^{-1} for magnesite and siderite, respectively).

In evaluating the change in $\delta^{13}\text{C}_{\text{raw}}$ across the twenty data acquisition cycles associated with each individual spot analysis, we noted moderately well-defined linear trends towards lower values in both Type-I and -II bias calibration data sets (i.e., fractionation in favour of the lighter isotope increased with time; see cycle-by-cycle plots in Appendix S4: Figures SA4-17 and SA4-20). Considering that the spot-to-spot repeatability of a $\delta^{13}\text{C}$ analysis is on the order of 0.6–1.2‰ (2s), the cumulative change in $\delta^{13}\text{C}_{\text{raw}}$ between the first and last cycle of analysis ($\Delta^{13}\text{C}(c_f - c_i)$) shows no resolvable dependence on Fe# in the case of the Type-II bias trend (average change of -4%). In contrast, a weak parabolic dependence was noted in association with the Type-I trend, where the cumulative change in $\Delta^{13}\text{C}(c_f - c_i)$ is smallest near the compositional mid-point of the solid-solution (approximately -2%) and largest near the end-members (approximately -4% ; see Figure 6b and additional examples from other sessions in Appendix S4: Figure SA4-16b).

Conclusions and recommendations

Recent advances in SIMS instrument design and refinements of analytical techniques have brought about the technical capability of performing highly precise, micrometre-scale *in situ* measurements of carbonate $\delta^{18}\text{O}$ and $\delta^{13}\text{C}$ values. The common spot-sizes employed for $\delta^{18}\text{O}$ analyses at WiscSIMS have diameters of 3- or 10- μm , affording repeatability precision at the following levels: $\pm 0.3\%$ (2s; 10- μm spots) and $\pm 0.7\%$ (2s; 3- μm spots). A 6- μm spot is used for $\delta^{13}\text{C}$ determinations, with repeatability precision between 0.6 and 1.2‰ (2s).

The accuracy of such measurements in relation to certified reference materials, however, depends in large part on the availability of comprehensive suites of matrix-matched reference materials that allow for characterising and calibrating sample matrix effects. This is entirely an empirical undertaking. With regard to Ca-Mg-Fe carbonates, this has been an under-researched topic since the first-

pioneering studies in the late 1990s (e.g., Eiler *et al.* 1997a, Valley *et al.* 1997, Riciputi *et al.* 1998). With this third instalment of our ongoing study of these effects, most of the common inorganic Ca-Mg-Fe carbonate compositions can now be accurately analysed. This includes calcite (Kozdon *et al.* 2009) and both the dolomite–ankerite (Parts I and II; Śliwiński *et al.* 2016a, b) and magnesite–siderite solid-solution series (Part III, this article). Biogenic carbonates may present additional complexity if organic matter, water or fine-grained, porous textures are present (Orland *et al.* 2015).

Following 2 years of RM development and of acquiring calibration data sets, we can at present offer the following observations, conclusions and recommendations regarding SIMS analysis of carbonates of the magnesite–siderite series:

- 1 As with the dolomite–ankerite series, mass bias was consistently most sensitive to changes in composition near the iron-free end-member of the solid-solution. With increasing Fe content up to ~ 20 mol% FeCO_3 end-member (Fe# 0.0–0.2, where Fe# = Fe/(Mg + Fe), expressed on a molar basis), $\delta^{13}\text{C}$ bias increased by up to 3–4.5‰, whereas $\delta^{18}\text{O}$ bias decreased by 13–15‰ (session-specific differences).
- 2 Between the end-members of the series, $\delta^{13}\text{C}$ bias increased by a total of 10–11‰ (magnesite \rightarrow siderite), whereas $\delta^{18}\text{O}$ bias decreased by 13–16‰ (session-specific differences).
- 3 As an example, if uncorrected, the presence of 1–2 mol% FeCO_3 in a sample material of unknown isotopic composition would produce a measurement error (in relation to CRM NIST-19) of $\sim 1\%$ for $\delta^{13}\text{C}$ and $\sim 2\text{--}3\%$ for $\delta^{18}\text{O}$ measurements.
- 4 Despite adherence to well-established analytical protocols for carbonate $\delta^{13}\text{C}$ and $\delta^{18}\text{O}$ analyses at WiscSIMS (CAMECA IMS 1280), the magnesite–siderite calibration curves of both isotope systems did not maintain a constant shape from session-to-session over a 2-year period, but rather fell into one of two distinct and largely self-consistent shape categories (Type-I' and Type-II').
- 5 The shape of Type-I and -II $\delta^{18}\text{O}$ bias trends differed most in the compositional space between Fe# = 0.3 and 0.9, where RM bias values changed on a session-by-session basis by: (a) up to 6‰ when using conditions for 10- μm diameter spot-size measurements; and (b) up to 4‰ when using 3- μm conditions.
- 6 The shape of Type-I and II $\delta^{13}\text{C}$ bias trends differ most in the compositional space between Fe# = 0.0 and 0.5, where RM bias values change on a session-by-session basis by up to 1–2‰.

7 The cause of variability in calibration curve shapes is not well understood at present, and stresses the importance of having available a sufficient number of well-characterised RMs so that potential complexities of curvature can be adequately delineated and accounted for on a session-by-session basis. Doing so allows for calibration residuals (a measure of accuracy in relation to CRM NIST-19) smaller than 0.5‰ for both isotope systems.

Acknowledgements

This material is based primarily upon work supported by the US Department of Energy Office of Science, Office of Basic Energy Sciences, Chemical Sciences, Geosciences, and Biosciences Division under award number DE-FG02-93ER14389. The WiscSIMS Laboratory is partly funded by the US National Science Foundation (EAR-1355590) and the University of Wisconsin-Madison. We express our gratitude to University of Wisconsin-Madison colleagues: N. Kita for providing guidance on SIMS analysis, J. Kern for instrumentation support, P. Sobol for constructive discussions and W. Schneider for assistance with SEM imaging. We warmly thank the following individuals and institutions for facilitating this research by supplying many of the mineral specimens that were assessed during the first three parts of this study, some of which were successfully developed into reference materials: P.W. Pohwat and the Smithsonian Institution (source of UWMgs6 [NMNH 96962] and UWAnk4 [NMNH 93418-08]), R.S. Bottrill and Mineral Resources Tasmania (source of UWMgs7), J.M. Eiler (material for UWSd5/JE-Mg-Sid and UWAnk7), J. Craven (material for UWSd1 / Ivig. Sid) and Josef Huber (<http://www.hubermineralien.jimdo.com>), who located and supplied the source materials for the RMs UWAnk5 cl, -5opq, -6a, and UWMgs2 and -3. We thank Richard Stern and an anonymous reviewer for a thorough and constructive review of this work.

References

- Allison C.E., Francey R.J. and Meijer H.A.J. (1995)**
Reference and intercomparison materials for stable isotopes of light elements. *IAEA-TECDOC*, 825, 155–162.
- Baertschi P. (1976)**
Absolute ^{18}O content of standard mean ocean water. *Earth and Planetary Science Letters*, 31, 341–344.
- Beukes N.J. and Klein C. (1990)**
Geochemistry and sedimentology of a facies transition – from microbanded to granular iron-formation – in the early Proterozoic Transvaal Supergroup, South Africa. *Precambrian Research*, 47, 99–139.
- Beukes N.J., Klein C., Kaufman A.J. and Hayes J.M. (1989)**
Carbonate petrography, kerogen distribution, and carbon and oxygen isotope variations in an early Proterozoic transition from limestone to iron-formation deposition, Transvaal Supergroup, South Africa. *Economic Geology and the Bulletin of the Society of Economic Geologists*, 85, 663–690.
- Blake D.F., Amundsen H.E.F., Benning L., Bish D., Conrad P., Fogel M., Midtkandal I., Ming D., Steele A., Treiman A.H. and AMASE Team (2010)**
Carbonate cements from the Sverrefjell and Sigurd fjell volcanoes, Svalbard Norway: Terrestrial analogs for Martian carbonates? *LPI Contributions*, 1538, 5119.
- Botz R.W. and von der Borch C.C. (1984)**
Stable isotope study of carbonate sediments from the Coorong area, South Australia. *Sedimentology*, 31, 837–849.
- Brodie M.W. (2016)**
Diagenesis and reservoir quality of the Middle Bakken Formation. PhD thesis (University of Durham, UK).
- Buckley H.A. and Woolley A.R. (1990)**
Carbonates of the magnesite–siderite series from four carbonatite complexes. *Mineralogical Magazine*, 54, 413–418.
- Burley S.D. and Worden R.H. (2003)**
Sandstone diagenesis: Recent and ancient. Blackwell Publishing (Malden, USA).
- Chai L. and Navrotsky A. (1996)**
Synthesis, characterization, and enthalpy of mixing of the (Fe, Mg)CO₃ solid solution. *Geochimica et Cosmochimica Acta*, 60, 4377–4383.
- Chang LL, Howie R.A. and Zussman J. (1996)**
Rock forming minerals, Volume 5B: Non-silicates: Sulphates, carbonates, phosphates, halides. Longman (Harlow, Essex), 383pp.
- Craig H. (1957)**
Isotopic standards for carbon and oxygen and correction factors for mass-spectrometric analysis of carbon dioxide. *Geochimica et Cosmochimica Acta*, 12, 133–149.
- Curtis C.D. (1995)**
Post-depositional evolution of mudstones I: Early days and parental influences. *Journal of the Geological Society of London*, 152, 577–586.
- Curtis C., Petrowski C. and Oertel G. (1972)**
Stable carbon isotope ratios within carbonate concretions – due to place and time of formation. *Nature*, 235, 98–100.
- Curtis C.D., Coleman M.L. and Love L.G. (1986)**
Pore water evolution during sediment burial from isotopic and mineral chemistry of calcite, dolomite and siderite concretions. *Geochimica et Cosmochimica Acta*, 50, 2321–2334.

references

Dobrzhinetskaya L.F., Green H.W., Mitchell T.E. and Dickerson R.M. (2001)

Metamorphic diamonds: Mechanism of growth and inclusion of oxides. *Geology*, 29, 263–266.

Donovan J.J. and Tingle T.N. (1996)

An improved mean atomic number background correction for quantitative microanalysis. *Microscopy and Microanalysis*, 2, 1–7.

Donovan J.J., Kremser D. and Fournelle J.H. (2007)

ProbeForWindows user's guide and reference (Enterprise Edition). Probe Software Inc. (Eugene, USA), 355pp.

Dworkin S.I., Nordt L. and Atchley S. (2005)

Determining terrestrial paleotemperatures using the oxygen isotopic composition of pedogenic carbonate. *Earth and Planetary Science Letters*, 237, 56–68.

Eiler J.M., Valley J.W. and Graham C.M. (1997a)

Standardization of SIMS analysis of O and C isotope ratios in carbonates from ALH84001. 28th Annual Lunar and Planetary Science Conference, 327.

Eiler J.M., Graham C. and Valley J.W. (1997b)

SIMS analysis of oxygen isotopes: Matrix effects in complex minerals and glasses. *Chemical Geology*, 138, 221–244.

Eiler J.M., Valley J.W., Graham C.M. and Fournelle J. (2002)

Two populations of carbonate in ALH84001: Geochemical evidence for discrimination and genesis. *Geochimica et Cosmochimica Acta*, 66, 1285–1303.

Fàbrega C., Parcerisa D., Rossell J.M., Gurenko A. and Franke C. (2017)

Predicting instrumental mass fractionation (IMF) of stable isotope SIMS analyses by response surface methodology (RSM). *Journal of Analytical Atomic Spectrometry*, 32, 731–748.

Fayek M., Harrison T.M., Grove M., McKeegan K.D., Coath C.D. and Boles J.R. (2001)

In situ stable isotopic evidence for protracted and complex carbonate cementation in a petroleum reservoir, North Coles Levee, San Joaquin Basin, California, USA. *Journal of Sedimentary Research*, 71, 444–458.

Fernández-Nieto C., Torres-Ruiz J., Pérez I.S., González I.F. and López J.G. (2003)

Genesis of Mg-Fe carbonates from the Sierra Menera magnesite-siderite deposits, northeast Spain: Evidence from fluid inclusions, trace elements, rare earth elements, and stable isotope data. *Economic Geology*, 98, 1413–1426.

Fitzsimons I.C.W., Harte B. and Clark R.M. (2000)

SIMS stable isotope measurement: Counting statistics and analytical precision. *Mineralogical Magazine*, 64, 59–83.

Frost M.T. (1982)

The magnesite deposit at Main Creek, Savage River, Tasmania. *Economic Geology*, 77, 1901–1911.

Gautier D.L. (1982)

Siderite concretions: Indicators of early diagenesis in the Gammon Shale (Cretaceous). *Journal of Sedimentary Research*, 52, 0859–0871.

Goutelle S., Maurin M., Rougier F., Barbaut X., Bourguignon L., Ducher M. and Maire P. (2008)

The Hill equation: A review of its capabilities in pharmacological modelling. *Fundamental and Clinical Pharmacology*, 22, 633–648.

Haroldson E.L. (2017)

Fluid inclusion and stable isotope study of Magino: A magmatic related Archean gold deposit. PhD thesis (University of Wisconsin-Madison).

Heimann A., Johnson C.M., Beard B.L., Valley J.W., Roden E.E., Spicuzza M.J. and Beukes N.J. (2010)

Fe, C, and O isotope compositions of banded iron formation carbonates demonstrate a major role for dissimilatory iron reduction in ~ 2.5 Ga marine environments. *Earth and Planetary Science Letters*, 294, 8–18.

Hervig R.L., Williams P., Thomas R.M., Schauer S.N. and Steele I.M. (1992)

Microanalysis of oxygen isotopes in insulators by secondary ion mass spectrometry. *International Journal of Mass Spectrometry and Ion Processes*, 120, 45–63.

Hill A.V. (1910)

The possible effects of the aggregation of the molecules of haemoglobin on its dissociation curves. *The Journal of Physiology*, 40, 4–7.

Huberty J.M., Kita N.T., Kozdon R., Heck P.R., Fournelle J.H., Spicuzza M.J., Xu H. and Valley J.W. (2010)

Crystal orientation effects in $\delta^{18}\text{O}$ for magnetite and hematite by SIMS. *Chemical Geology*, 276, 269–283.

Hunt C.P., Moskowitz B.M. and Banerjee S.K. (1995)

Magnetic properties of rocks and minerals. In: Ahrens T.J. (ed.), AGU Reference Shelf. Rock physics and phase relations – A handbook of physical constants, vol. 3. American Geophysical Union, 189–204.

Ickert R.B. and Stern R.A. (2013)

Matrix corrections and error analysis in high-precision SIMS $^{18}\text{O}/^{16}\text{O}$ measurements of Ca-Mg-Fe garnet. *Geostandards and Geoanalytical Research*, 37, 429–448.

Isa J., Kohl I.E., Liu M.-C., Wasson J.T., Young E.D. and McKeegan K.D. (2017)

Quantification of oxygen isotope SIMS matrix effects in olivine samples: Correlation with sputter rate. *Chemical Geology*, 458, 14–21.

James H.L. (1954)

Sedimentary facies of iron-formation. *Economic Geology*, 49, 235–293.

Johnson C.M., Ludois J.M., Beard B.L., Beukes N.J. and Heimann A. (2013)

Iron formation carbonates: Paleocceanographic proxy or recorder of microbial diagenesis? *Geology*, 41, 1147–1150.



references

- Kaminsky F.V., Wirth R. and Schreiber A. (2013)**
Carbonatitic inclusions in deep mantle diamond from Juina, Brazil: New minerals in the carbonate-halide association. *The Canadian Mineralogist*, 51, 669–688.
- Kaufman A., Hayes J. and Klein C. (1990)**
Primary and diagenetic controls of isotopic compositions of iron-formation carbonates. *Geochimica et Cosmochimica Acta*, 54, 3461–3473.
- Kita N.T., Ushikubo T., Fu B. and Valley J.W. (2009)**
High precision SIMS oxygen isotope analysis and the effect of sample topography. *Chemical Geology*, 264, 43–57.
- Kita N.T., Huberty J.M., Kozdon R., Beard B.L. and Valley J.W. (2011)**
High-precision SIMS oxygen, sulfur and iron stable isotope analyses of geological materials: Accuracy, surface topography and crystal orientation. *Surface and Interface Analysis*, 43, 427–431.
- Kitajima K., Strickland A., Spicuzza M.J. and Valley J.W. (2015)**
Improvement in matrix correction of $\delta^{18}\text{O}$ analysis by SIMS for pyralisite and Cr-pyrope garnet. *High Resolution Proxies of Paleoclimate 2015 Meeting (HiRes2015)*, WiscSIMS Laboratory, University of Wisconsin-Madison. http://www.geology.wisc.edu/~wiscsims/HiRes2015/posters/HiRes2015_Kitajima.pdf (Accessed October 31, 2017).
- Klein C. (2005)**
Some Precambrian banded iron-formations (BIFs) from around the world: Their age, geologic setting, mineralogy, metamorphism, geochemistry, and origins. *American Mineralogist*, 90, 1473–1499.
- Kozdon R., Ushikubo T., Kita N.T., Spicuzza M. and Valley J.W. (2009)**
Intratest oxygen isotope variability in the planktonic foraminifer *N. pachyderma*: Real vs. apparent vital effects by ion microprobe. *Chemical Geology*, 258, 327–337.
- Ludvigson G.A., González L.A., Metzger R.A., Witzke B.J., Brenner R.L., Murillo A.P. and White T.S. (1998)**
Meteoric sphaerosiderite lines and their use for paleohydrology and paleoclimatology. *Geology*, 26, 1039–1042.
- Ludvigson G.A., Gonzalez L.A., Fowle D.A., Roberts J.A., Driese S.G., Villarreal M.A., Smith J.J. and Suarez M.B. (2013)**
Paleoclimatic applications and modern process studies of pedogenic siderite. In: Driese S.G. and Nordt L.C. (eds), *New frontiers in paleopedology and terrestrial paleoclimatology: Paleosols and soil surface analog systems*. SEPM (Tulsa), 79–87.
- Lugli S., Morteani G. and Blamart D. (2002)**
Petrographic, REE, fluid inclusion and stable isotope study of magnesite from the Upper Triassic Burano evaporites (Secchia Valley, northern Apennines): Contributions from sedimentary, hydrothermal and metasomatic sources. *Mineralium Deposita*, 37, 480–494.
- Luzón A., Mayayo M.J. and Pérez A. (2009)**
Stable isotope characterisation of co-existing carbonates from the Holocene Gallocanta lake (NE Spain): Palaeolimnological implications. *International Journal of Earth Sciences*, 98, 1129–1150.
- Macquaker J.H.S., Curtis C.D. and Coleman M.L. (1997)**
The role of iron in mudstone diagenesis; comparison of Kimmeridge Clay Formation mudstones from onshore and offshore (UKCS) localities. *Journal of Sedimentary Research*, 67, 871–878.
- Mayayo M.J., Bauluz B., López-Galindo A. and González-López J.M. (1996)**
Mineralogy and geochemistry of the carbonates in the Calatayud Basin (Zaragoza, Spain). *Chemical Geology*, 130, 123–136.
- McCrea J.M. (1950)**
On the isotopic chemistry of carbonates and a paleotemperature scale. *The Journal of Chemical Physics*, 18, 849.
- McGrail B.P., Schaef H.T., Spang F.A., Cliff J.B., Qafoku O., Homer J.A., Thompson C.J., Owen A.T. and Sullivan C.E. (2016)**
Field validation of supercritical CO_2 reactivity with basalts. *Environmental Science and Technology Letters*, 4, 6–10.
- Mees F. and Keppens E. (2013)**
Stable isotope geochemistry of magnesite from Holocene salt lake deposits, Taoudenni, Mali. *Geological Journal*, 48, 620–627.
- Morad S. (1998)**
Carbonate cementation in sandstones: Distribution patterns and geochemical evolution. In: Morad S. (ed.), *Carbonate cementation in sandstones*. Blackwell Publishing (Oxford, UK), 1–26.
- Morris R.V., Blake D.F., Bish D., Ming D.W., Agresti D.G., Treiman A.H., Steele A. and Amundsen H.E.F. (2011)**
A terrestrial analogue from Spitsbergen (Svalbard, Norway) for the Comanche Carbonate at Gusev Crater, Mars. *LPI Contribution No. 1608*, 1699.
- Mozley P.S. (1989a)**
Complex compositional zonation in concretionary siderite: Implications for geochemical studies. *Journal of Sedimentary Research*, 59, 815–818.
- Mozley P.S. (1989b)**
Relation between depositional environment and the elemental composition of early diagenetic siderite. *Geology*, 17, 704–706.
- Niles P.B., Catling D.C., Berger G., Chassefière E., Ehlmann B.L., Michalski J.R., Morris R., Ruff S.W. and Sutter B. (2013)**
Geochemistry of carbonates on Mars: Implications for climate history and nature of aqueous environments. *Space Science Reviews*, 174, 301–328.
- Orland I.J., Kozdon R., Linzmeier B., Wycech J., Śliwiński M., Kitajima K., Kita N.T. and Valley J.W. (2015)**
Enhancing the accuracy of carbonate $\delta^{18}\text{O}$ and $\delta^{13}\text{C}$ measurements by SIMS. *AGU Fall 2015 Meeting (San Francisco, USA)*, Paper number: PP52B-03.

references

- Page F.Z., Kita N.T. and Valley J.W. (2010)**
Ion microprobe analysis of oxygen isotopes in garnets of complex chemistry. *Chemical Geology*, 270, 9–19.
- Perry E.C., Tan F.C. and Morey G.B. (1973)**
Geology and stable isotope geochemistry of the Biwabik Iron Formation, northern Minnesota. *Economic Geology*, 68, 1110–1125.
- Postma D. (1982)**
Pyrite and siderite formation in brackish and freshwater swamp sediments. *American Journal of Science*, 282, 1151–1183.
- Power I. and Southam G. (2005)**
Carbon dioxide sequestration through enhanced weathering of chrysotile mine tailings and subsequent microbial precipitation of magnesium carbonates. *Geochimica et Cosmochimica Acta*, Supplement, 69, 834.
- Power I.M., Harrison A.L., Dipple G.M., Wilson S.A., Kelemen P.B., Hirth M. and Southam G. (2013)**
Carbon mineralization: From natural analogues to engineered systems. *Reviews in Mineralogy and Geochemistry*, 77, 305–360.
- Riciputi L.R., Paterson B.A. and Ripperdan R.L. (1998)**
Measurement of light stable isotope ratios by SIMS: Matrix effects for oxygen, carbon, and sulfur isotopes in minerals. *International Journal of Mass Spectrometry*, 178, 81–112.
- Rochette P. (1988)**
Inverse magnetic fabric in carbonate-bearing rocks. *Earth and Planetary Science Letters*, 90, 229–237.
- Rosenbaum J. and Sheppard S.M.F. (1986)**
An isotopic study of siderites, dolomites and ankerites at high temperatures. *Geochimica et Cosmochimica Acta*, 50, 1147–1150.
- Sanz-Montero M.E. and Rodríguez-Aranda J.P. (2012)**
Magnesite formation by microbial activity: Evidence from a Miocene hypersaline lake. *Sedimentary Geology*, 263–264, 6–15.
- Schmidt V., Günther D. and Hirt A.M. (2006)**
Magnetic anisotropy of calcite at room-temperature. *Tectonophysics*, 418, 63–73.
- Schmidt V., Hirt A.M., Hametner K. and Günther D. (2007)**
Magnetic anisotropy of carbonate minerals at room temperature and 77K. *American Mineralogist*, 92, 1673–1684.
- Sheldon N.D. and Tabor N.J. (2009)**
Quantitative paleoenvironmental and paleoclimatic reconstruction using paleosols. *Earth-Science Reviews*, 95, 1–52.
- Śliwiński M.G., Kitajima K., Kozdon R., Spicuzza M.J., Fournelle J.H., Denny A. and Valley J.W. (2016a)**
Secondary ion mass spectrometry bias on isotope ratios in dolomite–ankerite, Part I: $\delta^{18}\text{O}$ Matrix effects. *Geostandards and Geoanalytical Research*, 40, 157–172.
- Śliwiński M.G., Kitajima K., Kozdon R., Spicuzza M.J., Fournelle J.H., Denny A. and Valley J.W. (2016b)**
Secondary ion mass spectrometry bias on isotope ratios in dolomite–ankerite, Part II: $\delta^{13}\text{C}$ Matrix effects. *Geostandards and Geoanalytical Research*, 40, 173–184.
- Śliwiński M.G., Kitajima K., Kozdon R., Spicuzza M.J., Denny A. and Valley J.W. (2017)**
In situ $\delta^{13}\text{C}$ and $\delta^{18}\text{O}$ microanalysis by SIMS: A method for characterizing the carbonate components of natural and engineered CO_2 -reservoirs. *International Journal of Greenhouse Gas Control*, 57, 116–133.
- Sobolev N.V., Kaminsky F.V., Griffin W.L., Yefimova E.S., Win T.T., Ryan C.G. and Botkunov A.I. (1997)**
Mineral inclusions in diamonds from the Sputnik kimberlite pipe, Yakutia. *Lithos*, 39, 135–157.
- Stern J.C., McAdam A.C., Ten Kate I.L., Bish D.L., Blake D.F., Morris R.V., Bowden R., Fogel M.L., Glamoclija M., Mahaffy P.R., Steele A. and Amundsen H.E.F. (2013)**
Isotopic and geochemical investigation of two distinct Mars analog environments using evolved gas techniques in Svalbard, Norway. *Icarus*, 224, 297–308.
- Suarez M.B., González L.A. and Ludvigson G.A. (2010)**
Estimating the oxygen isotopic composition of equatorial precipitation during the mid-Cretaceous. *Journal of Sedimentary Research*, 80, 480–491.
- Tabor N.J. and Myers T.S. (2015)**
Paleosols as indicators of paleoenvironment and paleoclimate. *Annual Review of Earth and Planetary Sciences*, 43, 333–361.
- Telford W.M., Geldart L.P. and Sheriff R.E. (1990)**
Electrical properties of rocks and minerals. In: Telford W.M., Geldart L.P. and Sheriff R.E. (eds), *Applied Geophysics*. Cambridge University Press (Cambridge, UK), 283–292.
- Treiman A.H., Amundsen H.E., Blake D.F. and Bunch T. (2002)**
Hydrothermal origin for carbonate globules in Martian meteorite ALH84001: A terrestrial analogue from Spitsbergen (Norway). *Earth and Planetary Science Letters*, 204, 323–332.
- Ufnar D.F., González L.A., Ludvigson G.A., Brenner R.L. and Witzke B.J. (2004)**
Diagenetic overprinting of the sphaerosiderite palaeoclimate proxy: Are records of pedogenic groundwater $\delta^{18}\text{O}$ values preserved? *Sedimentology*, 51, 127–144.
- Valley J.W. and Kita N.T. (2009)**
In situ oxygen isotope geochemistry by ion microprobe. In: Fayek M. (ed.), *Secondary ion mass spectrometry in the Earth sciences: Gleaning the big picture from a small spot*. Mineralogical Association of Canada. Short Course, 41, 19–63.



references

Valley J.W., Eiler J.M., Graham C.M., Gibson E.K., Romanek C.S. and Stolper E.M. (1997)

Low-temperature carbonate concretions in the Martian meteorite ALH84001: Evidence from stable isotopes and mineralogy. *Science*, 275, 1633–1638.

Verkouteren R.M. and Klinedinst D.B. (2004)

Value assignment and uncertainty estimation of selected light stable isotope reference materials. *NIST Special Publication*, 260, 149.

VIM (2008)

International vocabulary of metrology – Basis and general concepts and associated terms (VIM). Joint Committee for Guides in Metrology, Bureau International des Poids et Mesures (Sèvres, France), 200:2008,90pp.

Wang A., Pasteris J.D., Meyer H.O.A. and Dele-Duboi M.L. (1996)

Magnesite-bearing inclusion assemblage in natural diamond. *Earth and Planetary Science Letters*, 141, 293–306.

Wilson S.A., Dipple G.M., Power I.M., Thom J.M., Anderson R.G., Raudsepp M., Gabites J.E. and Southam G. (2009)

Carbon dioxide fixation within mine wastes of ultramafic-hosted ore deposits: Examples from the Clinton Creek and Cassiar chrysotile deposits, Canada. *Economic Geology*, 104, 95–112.

Supporting information

The following supporting information may be found in the online version of this article:

Appendix S1. Results of conventional phosphoric acid digestion and gas source mass spectrometric analyses performed on the magnesite-siderite RMs of this study.

Appendix S2. Supplementary electron probe microanalysis data table.

Appendix S3. Complete SIMS datasets for all reported measurement sessions.

Appendix S4. Graphical description of the influence of the curve-shape parameters n , k , and d on Equation 6, along with additional examples of calibration curves and corresponding cycle-by-cycle data.

This material is available as part of the online article from: <https://onlinelibrary.wiley.com/doi/10.1111/ggr.12194/abstract> (This link will take you to the article abstract).